AD-A248 940

‖‖‖‖‖‖‖‖‖‖‖‖‖‖‖‖

PL-TR-91-2297

RESEARCH IN REGIONAL SEISMOLOGY: THE EFFECT OF ANISOTROPY

Richard L. Gibson, Jr.
M. Nafi Toksöz

Earth Resources Laboratory
Department of Earth, Atmospheric, and
    Planetary Sciences
Massachusetts Institute of Technology
Cambridge, MA 02139

19 November 1991

Scientific Report No. 1

APPROVED FOR PUBLIC RELEASE; DISTRIBUTION UNLIMITED

PHILLIPS LABORATORY
AIR FORCE SYSTEMS COMMAND
HANSCOM AIR FORCE BASE, MA 01731-5000

92 4 14 028

92-09600

‖‖‖‖‖‖‖‖‖‖‖‖‖‖‖

The views and conclusions contained in this document are those of the authors and should not be interpreted as representing the official policies, either expressed or implied, of the Air Force or the U.S. Government.

This technical report has been reviewed and is approved for publication.
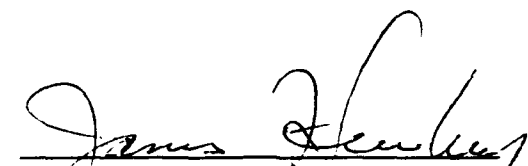
JAMES F. LEWKOWICZ
Contract Manager
Solid Earth Geophysics Branch
Earth Sciences Division
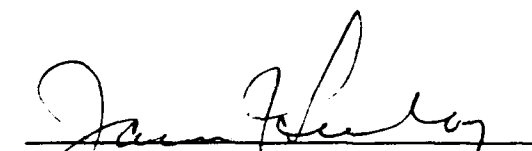
JAMES F. LEWKOWICZ
Branch Chief
Solid Earth Geophysics Branch
Earth Sciencs Division

DONALD H. ECKHARDT, Director
Earth Sciences Division

This document has been reviewed by the ESD Public Affairs Office (PA) and is releasable to the National Technical Information Service (NTIS).

Qualified requestors may obtain additional copies from the Defense Technical Information Center. All others should apply to the National Technical Information Service.

If your address has changed, or if you wish to be removed from the mailing list, or if the addressee is no longer employed by your organization, please notify PL/IMA, Hanscom AFB MA 01731-5000. This will assist us in maintaining a current mailing list.

Do not return copies of this report unless contractual obligations or notices on a specific document requires that it be returned.

REPORT DOCUMENTATION PAGE

Public reporting burden for this collection of information is estimated to average 1 hour per response, including the time for reviewing instructions, searching existing data sources, gathering and maintaining the data needed, and completing and reviewing the collection of information. Send comments regarding this burden estimate or any other aspect of this collection of information, including suggestions for reducing this burden, to Washington Headquarters Services, Directorate for Information Operations and Reports, 1215 Jefferson Davis Highway, Suite 1204, Arlington, VA 22202-4302, and to the Office of Management and Budget, Paperwork Reduction Project (0704-0188), Washington, DC 20503

1. AGENCY USE ONLY (Leave blank)	2. REPORT DATE 19 November 1991	3. REPORT TYPE AND DATES COVERED Scientific No. 1

4. TITLE AND SUBTITLE

Research in Regional Seismology: The Effect of Anisotropy

6. AUTHOR(S)

M. Nafi Toksöz
Richard L. Gibson, Jr.

5. FUNDING NUMBERS

F19628-90-K-0057
PE 62101F
PR 7600
TA 09
WU AY

7. PERFORMING ORGANIZATION NAME(S) AND ADDRESS(ES)

Earth Resources Laboratory
Dept. of Earth, Atmospheric, and Planetary Sciences
Massachusetts Institute of Technology
77 Massachusetts Avenue
Cambridge, MA 02139

8. PERFORMING ORGANIZATION REPORT NUMBER

74527

9. SPONSORING / MONITORING AGENCY NAME(S) AND ADDRESS(ES)

Phillips Laboratory
Hanscom AFB, MA 01731-5000

Contract Manager: James Lewkowicz/GPEH

10. SPONSORING / MONITORING AGENCY REPORT NUMBER

PL-TR-91-2297

11. SUPPLEMENTARY NOTES

12a. DISTRIBUTION / AVAILABILITY STATEMENT

Approved for Public Release; Distribution Unlimited

12b. DISTRIBUTION CODE

13. ABSTRACT (Maximum 200 words)

The objective of this study is to examine the influence of fracturing and anisotropy in the source medium or near the source on radiation, especially the generation of SV and SH. One effect is scattering near the source. We present a ray-Born method for the computation of scattered wavefields in a general 3-D, anisotropic medium. This approach applies ray methods to the computation of Green's tensors for a background earth model and uses the Born approximation to determine the scattered wavefield from each volume element within a discretized model of heterogeneity. The application of these two approximate methods requires that the background model be relatively smooth compared to a wavelength for the validity of ray theory, but that the scattering heterogeneity have short characteristic length compared to the propagating wavelength for accurate use of the Born approximation. Comparisons of ray-Born results to the complete solution for scattering from an elastic sphere show that this method works fairly well for wavelengths on the order of five times larger than the length scales typical of the heterogeneity, but then breaks down due to the failure of the Born approximation. With this restriction in mind, the method is applied to a hypothetical layered earth model containing a thin, laterally extensive fracture zone.

14. SUBJECT TERMS

Anisotropy; fractures; scattering

15. NUMBER OF PAGES

84

16. PRICE CODE

17. SECURITY CLASSIFICATION OF REPORT	18. SECURITY CLASSIFICATION OF THIS PAGE	19. SECURITY CLASSIFICATION OF ABSTRACT	20. LIMITATION OF ABSTRACT
UNCLASSIFIED	UNCLASSIFIED	UNCLASSIFIED	SAR

NSN 7540-01-280-5500

Table of Contents

Accession For
NTIS GRA&I
DTIC TAB
Unannounced
Justification

By
Distribution/
Availability Codes
Dist | Avail and/or
Special
A-1

List of Contributing Scientists

Richard L. Gibson, Jr., Graduate Research Assistant, Massachusetts Institute of
Technology

M. Nafi Toksöz, Professor of Geophysics, Massachusetts Institute of Technology

List of Previous and Related Contracts

DARPA/GL Contract F19628-88-K-0036, "Seismic Wave Propagation, Attenuation and
Scattering over Regional Distances", August 1988 to July 1989.

DARPA/AFGL Contract F19628-89-K-0020 "Regional Seismograms: Attenuation and
Scattering", July 1989 to June 1991.

Bibliography of Publications Totally or Partially Supported by the Contract

Toksöz, M.N., B. Mandal, R.L. Gibson, Jr., and A.M. Dainty, 1991. Research in
regional seismology: the effect of anisotropy. *Papers Presented at 13th Ann.
PL/DARPA Seismic Res. Symp.*, 445-452. PL-TR-91-2208, ADA241325.

Gibson, R.L., Jr., and M.N. Toksöz, 1991. Ray-Born synthetic seismograms for 3-D,
anisotropic, and inhomogeneous media: applications to fracture zones. *Submitted
to Geophys. J. Int.*

Preface

The objective of this new study is an examination of the influence of fracturing and anisotropy in the source medium or near the source on radiation patterns from explosions, including the generation of SV and SH. In previous work under other contracts we have studied radiation patterns of P and S waves for explosions set off in anisotropic media, especially for cases that mimic earthquakes and/or generate SH waves. This report consists of a manuscript submitted to *Geophysical Journal International* presenting a formalism for calculating the effects of scattering from fracture zones of material, such as might be found near the source in a test site.

RAY-BORN SYNTHETIC SEISMOGRAMS FOR 3-D, ANISOTROPIC, AND INHOMOGENEOUS MEDIA: APPLICATIONS TO FRACTURE ZONES

Richard L. Gibson, Jr. and M. Nafi Toksöz

Earth Resources Laboratory

Department of Earth, Atmospheric, and Planetary Sciences

Massachusetts Institute of Technology

Cambridge MA 02139

ABSTRACT

We present a ray-Born method for the computation of scattered wavefields in a general 3-D, anisotropic medium. This approach applies ray methods to the computation of Green's tensors for a background earth model and uses the Born approximation to determine the scattered wavefield from each volume element within a discretized model of heterogeneity. The application of these two approximate methods requires that the background model be relatively smooth compared to a wavelength for the validity of ray theory, but that the scattering heterogeneity have short characteristic length compared to the propagating wavelength for accurate use of the Born approximation. Comparisons of ray-Born results to the complete solution for scattering from an elastic sphere show that this method works fairly well for wavelengths on the order of five times larger than the length scales typical of the heterogeneity, but then breaks down due to the failure of the Born approximation. With this restriction in mind, the method is applied to a hypothetical layered earth model containing a thin, laterally extensive fracture zone. The results show that scattering from shear waves gives unique information on fracture orientation, since the properties of the reflected events depend significantly on the orientation of the incident S-wave polarization with respect to the fractures. For example, as the polarization of an incident SH-wave varies from perpendicular to parallel to aligned vertical fractures. the scattered wave amplitude decreases to zero. In intermediate directions, the polarization of the scattered wave includes some SV energy. On the other hand, compressional wave reflections show essentially no variation with orientation of the fractures. Modeling of waves scattered from fracture zones in VSP data from the Larderello geothermal field in Italy demonstrates the applicability of the method to modeling of field data and suggests that at least in this locality, anisotropic fracturing is not completely responsible for the observations. Analysis of the Fresnel zones affecting reflections from the thin fracture zones responsible for the scattering allows a delineation of regions of more intense fracturing, which is important for the development of geothermal resources.

2

INTRODUCTION

The modeling of seismic wave propagation to understand the effects of various earth struc-tures on observations and, conversely, to infer rock properties from data is hindered by the complexity of geological materials. In many cases, the geologic structures of interest are small compared to the three-dimensional volume through which the waves are transmitted, leading to practical difficulties in the implementation of numerical schemes, such as finite differences. Wave propagation is also complicated in many cases by anisotropy, which may be an inherent anisotropy of the minerals or an effective anisotropy due to the presence of a stack of thin isotropic layers (Crampin, 1981). Either of these effects usually leads to a transversely isotropic medium with a vertical axis of symmetry. Another important source of effective anisotropy in the crust is the alignment of fractures in an otherwise isotropic and ho-mogeneous layer, also leading to a transversely isotropic medium (Bamford and Nunn, 1979; Crampin, 1981; Crampin *et al.,* 1986; Leary *et al.,* 1987). Frequently the least principal stress is known through geological, seismological or borehole observations to be horizontal at depth (Zoback and Zoback, 1980; Jamison and Cook, 1980; Hickman *et al.,* 1988; Evans *et al.,* 1989), and this configuration results in a vertical alignment of cracks. The medium then has a horizontal axis of symmetry.

There have been many analyses of the effects of fractured layers of the earth on synthetic seismograms or field data (Crampin, 1978; Crampin, 1981; Crampin and McGonigle, 1985; Leary and Henyey, 1985; Martin and Davis, 1987; Ben-Menahem and Sena, 1990; Mandal and Toksöz, 1990; Spencer and Chi, 1991; Mueller, 1991). Most of these studies focus on the effects of shear wave splitting and the consequent anomalies in the polarization of observed shear wave data. These approaches are very successful in locations where the fractured, anisotropic region is relatively thick. In these areas, the two quasi-shear waves are observed at the receiver location with enough separation in time that they can be uniquely identified.

However, it is not realistic to suggest that the earth is everywhere uniformly fractured.

Many practical problems require the location of relatively small fracture zones within the surrounding bedrock. Some important examples of such problems are the location of fractures for the development of geothermal fields (Leary and Henyey, 1985; Batini et al., 1985a; Batini et al., 1991), for nuclear waste disposal (Green and Mair, 1983; Carswell and Moon, 1985), or for other purposes (Juhlin et al., 1991). These are examples of situations where the dimensions of the fracture zones are often not sufficiently thick that shear wave splitting will be detectable, even if the zone is anisotropic. Therefore, a different form of evidence for the fracturing must be sought in seismic data.

To achieve this objective, we apply a ray-Born computation of synthetic seismograms to model the scattering of elastic waves by relatively small features in three-dimensional structures. This approach is similar to that of Beydoun and Mendes (1989), who outline a ray-Born algorithm for migration or inversion problems in three-dimensional, isotropic media with examples of application to two-dimensional problems. Two basic approximations are employed to compute the wavefields expected for relatively complicated media. First, ray theory is used to compute the Green's tensors for a background earth model. Because asymptotic ray theory is employed, this background reference model must be sufficiently smooth that the high frequency assumption is valid (Ben-Menahem and Beydoun, 1985). Ray tracing has the advantage of allowing the computation of Green's tensors for large, three-dimensional models with minimal computation time. The second step is to use the Born approximation to compute the elastic waves generated by perturbations to the reference model, a method which expresses the effects of the perturbations as secondary sources radiating energy as they are encountered by the wave propagating in the background medium (Gubernatis et al., 1977; Wu and Aki, 1985; Gibson and Ben-Menahem, 1991). Application of this approximation is valid only for small, short wavelength features of an earth model. We show how the ray-Born method can be extended to fully general anisotropic and inhomogeneous earth models using the high frequency Green's tensor for anisotropic background media (Ben-Menahem et al., 1990) and the expressions for the secondary source radiation

4

by anisotropic perturbations developed in Gibson and Ben-Menahem (1991). We apply the method to three-dimensional isotropic earth models with anisotropic perturbations.

After describing the ray-Born algorithm, including a brief review of the Born approximation, we explore the question of the accuracy of the Born approximation in computing the scattered waves caused by varying degrees of heterogeneity. This is accomplished by comparing the ray-Born results with the complete solution for waves scattered from an elastic sphere by an incident plane P-wave. Using the guidelines for application of the ray-Born algorithm developed by this comparison, we next examine the wavefields generated by a thin but laterally extensive fracture zone in a hypothetical layered earth model to gain an understanding of the effects of fracture orientation on seismic waves in an ideal case. Lastly, we examine a set of VSP data from the Larderello geothermal field in Italy, where an important objective in the course of exploitation of geothermal resources is the delineation of thin fracture zones several kilometers in depth. We present a fracture zone model that explains the observed data and discuss the implications of the results to determine fracture alignment in the Larderello field based on the synthetic results from our model.

COMPUTATION OF THE BORN SCATTERED FIELD

The Born Integral Equation

The vector form of the source free equation of motion for an inhomogeneous medium is

$$\rho \ddot{u} - \nabla \cdot \mathbf{T} = 0, \tag{1}$$

where ρ is density, u is the displacement vector, and $\mathbf{T}$ is the stress tensor (Ben-Menahem and Singh, 1981). Derivatives with respect to time are indicated by the dot symbols over the vector u. Hooke's law relates the stress tensor and the strain tensor $\mathbf{E}$ through the fourth-order elastic tensor c:

$$\mathbf{T} = \mathbf{c} : \mathbf{E}. \tag{2}$$

5

The elastic tensor obeys the usual symmetry relationships

$$c_{ijkl} = c_{klij} = c_{jikl} = c_{ijlk},\qquad(3)$$

resulting in a total of 21 independent elastic constants.

The Born approximation to the scattered field generated by heterogeneous materials is obtained by considering perturbations of the elastic properties of a prescribed background reference model:

$$\rho(\mathbf{x}) = \rho^0(\mathbf{x}) + \delta\rho(\mathbf{x})$$
$$c_{ijkl}(\mathbf{x}) = c^0_{ijkl}(\mathbf{x}) + \delta c_{ijkl}(\mathbf{x}).\qquad(4)$$

Here the superscript ^{0} indicates a value of the known background model and $\mathbf{x}$ is the position vector. The values $\delta\rho(\mathbf{x})$ and $\delta c_{ijkl}(\mathbf{x})$ are the perturbations to the reference values $\rho^0(\mathbf{x})$ and $c^0_{ijkl}(\mathbf{x})$. Both the background and perturbation models are taken to be functions of location $\mathbf{x}$. Derivation of expressions for the scattered field proceeds by assuming that the displacement field in the total medium is also given by the sum of the field $\mathbf{u}^0(\mathbf{x})$ which would propagate in the background material and a scattered field $\delta\mathbf{u}(\mathbf{x})$:

$$\mathbf{u}(\mathbf{x},t) = \mathbf{u}^0(\mathbf{x},t) + \delta\mathbf{u}(\mathbf{x},t).\qquad(5)$$

Gibson and Ben-Menahem (1991) show that substitution of equations (4) and (5) into the equation of motion (1), neglecting second-order terms, yields a solution for the scattered field

$$\delta\mathbf{u}(\mathbf{x},t) = \int dV(\mathbf{x}') \int dt'\ \mathbf{G}^0(\mathbf{x},t;\mathbf{x}',t') \cdot (\delta\rho\ddot{\mathbf{u}}^0(\mathbf{x}',t'))$$
$$+ \int dV(\mathbf{x}') \int dt'\ [\delta\mathbf{c}(\mathbf{x}',t') : \mathbf{E}^0(\mathbf{x}',t')] : \nabla\widetilde{\mathbf{G}^0}(\mathbf{x},t;\mathbf{x}',t').\qquad(6)$$

The $\sim$ symbol indicates transpose of the Green's tensor $\mathbf{G}^0$. This Born approximation provides an approximation to the scattered field in terms of the incident wavefield $\mathbf{u}^0(\mathbf{x}.t)$ propagating in the background medium, as $\mathbf{E}^0(\mathbf{x}',t')$ is the strain associated with this displacement. $\mathbf{G}^0(\mathbf{x},t;\mathbf{x}',t')$ is the Green's tensor for the background earth model, with component

6

$G_{ij}^0(\mathbf{x},t;\mathbf{x}',t')$ representing the i component disturbance at location $\mathbf{x}$ from a source applied at $\mathbf{x}'$ in the $\mathbf{x_j}$ direction. The perturbations to the material quantities act as secondary sources for displacement fields propagating in the reference model, where the product of density perturbation and acceleration vector yields a single-force source vector at each point $\mathbf{x}'$ and time t'. Likewise, perturbations to the elastic tensor $\mathbf{c}$ result in double-force source terms which are doubly contracted against $\mathbf{G}^0(\mathbf{x},t;\mathbf{x}',t')$. This moment tensor type source $\delta M_{ij} = \delta c_{ijkl}E_{kl}$ is more easily interpreted by writing it in the following form, employing the standard Voigt notation:

$$
\begin{bmatrix} \delta M_{11} \\ \delta M_{22} \\ \delta M_{33} \\ \delta M_{23} \\ \delta M_{13} \\ \delta M_{12} \end{bmatrix} = \begin{bmatrix} \delta C_{11} & \delta C_{12} & \delta C_{13} & \delta C_{14} & \delta C_{15} & \delta C_{16} \\ & \delta C_{22} & \delta C_{23} & \delta C_{24} & \delta C_{25} & \delta C_{26} \\ & & \delta C_{33} & \delta C_{34} & \delta C_{35} & \delta C_{36} \\ & & & \delta C_{44} & \delta C_{45} & \delta C_{46} \\ & & & & \delta C_{55} & \delta C_{56} \\ & & & & & \delta C_{66} \end{bmatrix} \begin{bmatrix} \epsilon_{11}^0 \\ \epsilon_{22}^0 \\ \epsilon_{33}^0 \\ 2\epsilon_{23}^0 \\ 2\epsilon_{13}^0 \\ 2\epsilon_{12}^0 \end{bmatrix}. \tag{7}
$$

In this expression, ϵ_{ij}^0 are the components of the strain tensor $\mathbf{E}^0(\mathbf{x}',t')$.

Evaluation of the Integral

Using equation (6), the Born scattered field for prescribed perturbations $\delta\rho$ and δc_{ijkl} can be computed once the incident field $\mathbf{u}^0(\mathbf{x},t)$ and its associated strain $\mathbf{E}^0(\mathbf{x}',t')$ are known. The Green's tensor $\mathbf{G}^0(\mathbf{x},t;\mathbf{x}',t')$ is the fundamental quantity which must be obtained, as it can be used to compute these background fields as well as the displacements generated by the secondary sources on the right-hand side of equation (6). Therefore, application of the integral solution first requires the knowledge of the Green's tensors for propagation in the background model and then an algorithm for the actual evaluation of the integral.

Following Beydoun and Mendes (1989), we proceed by discretizing the perturbed volume of the earth model (Figure 1). Each unit cell within the discretization is a rectangular

prism with dimensions dx_1, dx_2, and dx_3. As long as the wavelength of the incident wave is much greater than the largest dimension dx_i, the scattering due to each individual elemental volume is equivalent to Rayleigh scattering, which reduces the integration over volume in equation (6) to a simple multiplication by the elemental volume $dV = dx_1 dx_2 dx_3$ for a given unit cell:

$$\delta \mathbf{u}(\mathbf{x}, t) = \delta V \int dt' \ \mathbf{G}^0(\mathbf{x}, t; \mathbf{x}', t') \cdot (\delta \rho \ddot{\mathbf{u}}^0(\mathbf{x}', t'))$$

$$+ \delta V \int dt' \ (\delta \mathbf{c}(\mathbf{0}, t') : \mathbf{E}^0(\mathbf{0}, t')) : \nabla \widetilde{\mathbf{G}^0}(\mathbf{x}, t; \mathbf{0}, t'), \qquad (8)$$

or, in component notation,

$$\delta u_i(\mathbf{x}, t) = \delta V \int dt' \ G_{ij}(\mathbf{x}, t; \mathbf{x}', t')(\delta \rho \ddot{u}_j{}^0(\mathbf{x}', t'))$$

$$+ \delta V \int dt' \ (\delta c_{jklm}(\mathbf{x}', t')\epsilon_{lm}^0(\mathbf{x}', t'))G_{ij,k}^0(\mathbf{x}, t; \mathbf{x}', t'). \qquad (9)$$

Under the condition of Rayleigh scattering, each cell in the perturbed volume therefore acts as a point source located at the center of the cell, indicated by the dots in Figure 1. The point source at each lattice point is equivalent to some combination of single or double forces as presented in equation (6). Evaluation of the integral is most easily accomplished by simply summing the contributions of each of the point sources within the scattering volume, which corresponds to the most elementary implementation of the definition of an integral in terms of the limit of a sum of increasingly finely discretized representations of the range of the integral (Budak and Fomin, 1983). As long as the discretization of the volume is sufficiently small, the evaluation of the integral by this means should be sufficiently accurate.

A constraint on the sizes of the discretization intervals dx_1, dx_2 and dx_3 is made by considering the dominant period of the incident wave and therefore the incident wavelength. Adequate construction of the scattered wave requires at least four samples per period of the wave. For a reflected (back scattered) wave, the interval between the signals by adjacent pixels will be $2dx_i/v$ for a wave propagating in the x_i direction at velocity v. To obtain an adequate sampling then requires that the spacing dx_i be less than or equal to 1/8 of the

8

wavelength. For nearly vertically travelling waves, this constraint will apply to dx_3. The intervals dx_1 and dx_2 can be somewhat larger, as the wavefront will be essentially tangent to the x_1-x_2 plane, and the integrand in equation (6) will vary much more slowly in these directions.

The application of this integration scheme then requires a knowledge of the Green's tensors corresponding to the wave propagation from the primary source to each elemental scattering volume, yielding the properties of each secondary point source, and also from the scattering volume to the receivers, which determines the scattered field from each point source. Ray methods provide a fast and flexible means for performing these calculations in general three-dimensional layered models. The principal requirement for ray solutions to be applicable is that the wavelength must be much less than the characteristic length scale of the background earth model (Ben-Menahem and Beydoun, 1985). For inhomogeneous and anisotropic media meeting this length scale requirement, the ray theoretical Green's tensor is given by (Ben-Menahem et $al.$, 1991)

$$\mathbf{G}^0(\mathbf{x}, t; \mathbf{x}', t') = \frac{1}{4\pi[v(\mathbf{x}_0)]^2} \left[\frac{\rho(\mathbf{x}_0)v(\mathbf{x}_0)\hat{J}(\mathbf{x}_0)}{\rho(\mathbf{x})v(\mathbf{x})\hat{J}(\mathbf{x})} \right]^{1/2} [\mathbf{g}(\mathbf{x})\mathbf{g}(\mathbf{x}_0)]\, \delta(\tau(\mathbf{x}|\mathbf{x}_0)), \qquad (10)$$

where $\mathbf{x}_0$ is the source position, $\mathbf{x}$ is the observation point, $v(\mathbf{x})$ is phase velocity, and $v(\mathbf{x})\hat{J}(\mathbf{x})$ is the Jacobian of the transformation from Cartesian coordinates x_i to ray coordinates γ_j, where $\hat{J}(\mathbf{x})$ is given by

$$\hat{J}(\mathbf{x}) = \left| \frac{\partial \mathbf{x}}{\partial \gamma_1} \times \frac{\partial \mathbf{x}}{\partial \gamma_2} \right|. \qquad (11)$$

The ray coordinates are specified to be the two take-off angles of the ray at the source, the declination angle ψ and the azimuthal angle ϕ (Figure 2). It is important to realize that this Green's tensor contains only quantities obtained in the course of normal ray tracing algorithms. It contains the effects of geometrical spreading on amplitudes through the ratio of Jacobians $v(\mathbf{x}_0)\hat{J}(\mathbf{x}_0)/v(\mathbf{x})\hat{J}(\mathbf{x})$, as well as the material properties at the source and receiver points. The scalar amplitude multiplies a dyad given by the outer product of the polarization

vectors at the source and at the observation position, reproducing the usual reciprocity of elastic wave propagation in inhomogeneous media, whereby exchange of source and receiver positions result in the equivalence (Ben-Menahem and Singh, 1981)

$$G_{ij}(\mathbf{x}, t; \mathbf{x}', t') = G_{ji}(\mathbf{x}', t'; \mathbf{x}, t). \tag{12}$$

This ray theoretical Green's tensor will not be able to model aspects of wave propagation such as caustics or shadow zones, a fundamental limitation of the high frequency approximation (Červený, 1985).

Given the general ray theoretical Green's tensor in equation (10), the ray-Born method could be applied to general anisotropic media with anisotropic inhomogeneity. However, as a first step, we consider only an isotropic, inhomogeneous background model with anisotropic inclusions in order to develop an understanding of the effects of localized anisotropic regions on elastic wave propagation. This also allows the utilization of the elegant dynamic ray tracing (DRT) techniques in the ray-centered coordinates q_I with basis vectors $\mathbf{e}_I$ (Figure 2) (Červený, 1985). The DRT involves, in addition to the standard determination of ray path and travel time (kinematic ray tracing, KRT), the integration of eight additional ordinary differential equations to obtain the 2 by 2 matrices $\mathbf{Q}$ and $\mathbf{P}$. These components of these matrices can be expressed as

$$Q_{IJ} = \frac{\partial q_I}{\partial \gamma_J} \tag{13}$$

$$P_{IJ} = \frac{1}{v^2} \frac{dQ_{IJ}}{d\tau}. \tag{14}$$

Here τ is the travel time along the ray, and $I, J = 1, 2$. The P_{IJ} are needed only to obtain Q_{IJ}.

The matrix $\mathbf{Q}$ is related to the curvature of the wavefront (Červený, 1985). Knowledge of the components of this matrix yields geometric spreading, which is proportional to det $\mathbf{Q}$. $\mathbf{Q}$ is also used for the application of the paraxial method, which allows extrapolation of travel time and polarization vectors from a central ray which has been obtained by integration

10

to nearby observation points. This results in significant savings in computation time, as the two-point ray tracing is avoided. In an application such as the ray-Born method where the incident wavefield must be known at a large number of points, this is an especially valuable feature. These paraxial ray tracing procedures are discussed in many references (e.g., Červený, 1985).

In addition to these more typical paraxial corrections, we also include a correction to the geometrical spreading amplitude factor which can be derived using geometrical arguments. The integration of both the KRT and DRT equations is dependent on the choice of initial values. but once these values are selected the integration of the ray equations governs all propagation effects along the ray path from the initial point, within the limitations of the validity of ray methods. Because the initial conditions can be chosen along an initial wavefront as easily as from a source point, it follows that the additional geometrical spreading from the wavefront at central ray point $\mathbf{x}'$ and time $\tau(\mathbf{x}')$ to the wavefront at observation point $\mathbf{x}$ and time $\tau(\mathbf{x}) + \Delta\tau$ is in a homogeneous, isotropic material equivalent to the distance between wavefronts $v\Delta\tau$. The total geometrical spreading is then

$$\det \mathbf{Q} + v\Delta\tau. \tag{15}$$

In an inhomogeneous material, this correction will be less accurate, but since the paraxial corrections can only be applied a relatively short distance from the central ray, it should not be a severe limitation; application of this correction can be restricted to homogeneous regions of a model. It should also be noted that in this formulation, the changes in reflection and transmission coefficients with the variation in incidence angles on interfaces from the central ray to the ray which would actually intersect the observation point are not included. This also should not be a severe limitation except possibly near critical angles.

Another useful aspect of the DRT is that the partial derivatives may be used in an iterative two-point ray tracing scheme for rays propagating from the source to fixed receiver locations. While this is not necessary for the calculation of synthetic seismograms, it is often

11

desirable for the determination of accurate ray paths and will yield more accurate results than the straight application of the paraxial method. Once a ray is traced with an initial source point x and take-off angles γ_1^0 and γ_2^0, the γ_1 and γ_2 corresponding to the ray arriving at the desired observation point can be estimated through

$$\gamma_I \approx \gamma_I^0 + (Q^{-1})_{IJ}q_J. \tag{16}$$

We apply this result to two steps in the ray-Born procedure. First, for the computation of the background synthetic seismograms, we perform an iterative, two-point ray tracing procedure where we shoot a fan of rays over some range of prescribed take-off angles. Beginning with the closest ray to each receiver, we repeatedly apply equation (16) until the ray arrives with some distance of the desired receiver point. For layered models, the ray arriving essentially at the receiver point can usually be determined in three or fewer iterations, providing a very rapid determination of ray paths for multiply reflected and transmitted rays. For more complicated models, the procedure may not converge well, in which case the straight paraxial method can be applied. The second application of equation (16) is in the computation of the Green's tensor. Since the dyad in equation (10) contains the polarization vector at both the source and receiver points, to compute the tensor using the paraxial method at the scattering lattice we employ (16) to correct the polarization at the start of the central ray to be approximately that of the ray joining the source point and scattering point. Červený et al. (1987) outline the conversion of the results for the polarization dyad in ray-centered coordinates to Cartesian coordinates. Both SH and SV waves are automatically included in this procedure applied in ray-centered coordinates.

The algorithm can be summarized as follows:

1. Synthetic seismograms are computed for the background model using the iterative two-point ray tracing technique or the paraxial method. Green's tensors are computed and then the desired primary source type is applied to compute the background displacement field.

12

2. Green's tensors are computed for propagation from the primary source to each elemental volume in the scattering region. The Green's tensors are also computed for propagation from the scattering lattice to receivers. It is generally more convenient to do the ray tracing from receivers to the scattering volume and then apply the principle of reciprocity, transposing the Green's tensors (Ben-Menahem and Singh, 1981). Paraxial corrections are applied to rays passing near scattering points to minimize the amount of ray tracing necessary.

3. Perturbations to the material properties are specified, and the integration of equation (6) is performed by summing the contribution of each point source within the scattering lattice. The scattered field resulting from this calculation is then added to the primary field to produce the final synthetic seismograms.

An advantage of this method is that the Green's tensors may be saved prior to the application of the primary source of the Born approximation. This makes possible rapid comparison of the effects of different primary sources or different material perturbations on the wavefields, as the ray tracing, the most time consuming part of the algorithm, need only be done once.

COMPARISON OF RAY-BORN RESULTS TO A KNOWN ANALYTIC SOLUTION

The preceding ray-Born algorithm is in principle very general and can be applied to a wide variety of three-dimensional earth models, both isotropic and anisotropic. As long as the ray tracing can be satisfactorily accomplished, the integral over volume of heterogeneity is simply computed by summation. However, prior to application of the method to general problems, it is desirable to have some knowledge as to the accuracy and validity of the resulting synthetic seismograms. For this purpose, we compare the ray-Born scattered field results for a spherical object to the known solution in terms of spherical harmonics. This

13

comparison was chosen because it provides a true 3-D test of the ray-Born method for an obstacle of finite extent. If the heterogeneity were of infinite volume, such as a thin layer, then a synthesis of ray-Born results in practical implementations would require a truncation of the range of the integral in equation (6) to some finite portion of the thin layer. In this case, the comparisons would have to simultaneously examine both the accuracy of the ray-Born method itself and the validity of truncating the range of integration, complicating the conclusions that could be drawn from the results.

The scattered displacement field generated by a monochromatic plane wave incident on an isotropic, elastic sphere in an infinite homogeneous medium was obtained by Ying and Truell (1956). Derivation of this solution begins by expressing the components of displacement for a planar P-wave incident along the z axis,

$$
\begin{aligned}
\mathbf{V}_i(x_3, t) &= \mathbf{v}_i(x_3, t) e^{i\omega t} \\
\mathbf{v}_i(x_3, t) &= \hat{x}_3 e^{-ik_i z},
\end{aligned}
\tag{17}
$$

in terms of an expansion of a potential ψ_i in spherical harmonics:

$$
\begin{aligned}
\mathbf{u}_i &= -\nabla \psi_i \\
\psi_i &= \frac{1}{k_i} \sum_{m=0}^{\infty} (-i)^{m+1} (2m+1) j_m(k_i r) P_m(\cos\theta).
\end{aligned}
\tag{18}
$$

In these expressions, $k_i = \omega\alpha$, where α is the compressional wave velocity in the infinite medium, j_m is the spherical Bessel function of the first kind, and P_m is the Legendre polynomial. Spherical coordinates r and θ are illustrated in Figure 3. The scattered displacements are given by

$$
\begin{aligned}
\mathbf{V}_s &= \mathbf{v}_s e^{i\omega t} \\
\mathbf{v}_s &= -\nabla \psi_s + \nabla \times \nabla \times (\hat{r} r \Pi_s),
\end{aligned}
\tag{19}
$$

where ψ_s and Π_s are the compressional and shear wave potentials respectively, with harmonic

14

expansions

$$\psi_s = \sum_{m=0}^{\infty} A_m h_m(k_i r) P_m(\cos\theta)$$

$$\Pi_s = \sum_{m=0}^{\infty} B_m h_m(\kappa_i r) P_m(\cos\theta). \tag{20}$$

Here h_m is the spherical Bessel function of the third kind, $\kappa_i = \omega\beta$ is the shear wave number, and A_m and B_m are the as yet unknown coefficients of the expansion. The displacement field inside the sphere is expressed in similar expansions. giving two more unknown coefficients C_m and D_m. Boundary conditions on continuity of stress and displacement are applied at the surface of the spherical obstacle, resulting in four simultaneous equations that must be solved for the coefficients in each term m in the expansions.

Since a general seismic signal is actually composed of contributions from multiple frequencies, we apply a discrete wavenumber algorithm to compute synthetic seismograms as follows. A range of discrete frequencies is specified, $f_i = \Delta f, 2\Delta f, 3\Delta f, ..., f_{nyq}$, where $f_{nyq} = 1/2\Delta t$ is the Nyquist frequency corresponding to the time domain sample interval Δt. Each frequency f_i corresponds to a wavenumber k_i. The boundary value problem is then solved at frequencies f_i for the coefficients A_m, B_m, C_m and D_m. At each frequency, the harmonic expansion is carried out to sufficiently high-order m_n that coefficients A_{m_n}, B_{m_n}, C_{m_n} and D_{m_n} are negligible compared to A_0, B_0, C_0 and D_0. The Bessel functions of the first and second kinds of arbitrary order are computed using a Miller's algorithm appropriately modified for spherical Bessel functions (Press *et al.*, 1988). Finally, after the scattered field r and θ components have been computed at each frequency, this impulse response is convolved with the spectrum of the incident plane wave signal through frequency domain multiplication. and an inverse FFT is applied to produce the time domain response. In this way, the full waveform elastic wave scattered field of the spherical obstacle can be computed for a general incident plane wave pulse.

A comparison of the ray-Born and discrete wavenumber algorithm results was made using a spherical object of radius $a = 0.5$ km surrounded by a ring of receivers at a distance of

15

40 km (Figure 4). This configuration of receivers allows a comparison of both forward (90°) and back scattering results (270°). The infinite medium velocities were $\alpha_0 = 4.5$ km/sec and $\beta_0 = 2.7$ km/sec, with density 2.67 g/cm³; velocities within the spherical region were set to $\alpha = 4.545$ km/s and $\beta = 2.727$ km/s, perturbations of 1%. Density was kept constant, so that only the elastic Lamé parameters were varied. For the ray-Born calculations, a $10 \times 10 \times 20$ lattice with spacings $dx_1 = dx_2 = 0.10$ km and $dx_3 = 0.05$ km was specified and centered on the origin (note that x_1, x_2, and x_3 correspond to x, y and z coordinates in Figure 4). A finer spacing in the z direction was used for accurate evaluation of the ray-Born integral since this was the direction of the incident wave propagation and thus the most rapid variation of the integrand. Amplitude and phase of the incident plane wave are constant in both x and y. The perturbations at all lattice points at a distance larger than 0.5 km were set to zero providing an approximation to the spherical inhomogeneity. For both methods, the source wavelet used was given by

$$s(t_i) = e^{-(\omega_0(t-t_0))^2/\gamma^2} \cos(\omega_0(t - t_0)), \tag{21}$$

where t_0 is the arrival time, $\omega_0 = 2\pi f_0$ contains the center frequency f_0, and γ is a free parameter which we set to three. The resulting radial component P-wave synthetic seismograms from the two methods for center frequencies of 0.25, 1, 2.5 and 5 Hz are compared in Figures 5 and 6. The important parameter to determine the validity of the Born approximation is the ratio of wavelength to sphere diameter $\eta = \lambda_i/d$. These frequencies we have examined, 0.25, 1, 2.5 and 5 Hz, provide ratios $\eta_p = 18$, 4.5, 1.8 and 0.9, respectively, for compressional waves. Examination of the results for $\eta_p = 18$ (Figures 5A, 6A) shows that the two solutions are very similar, which is not surprising as this long wavelength reproduces the Rayleigh scattering result, where the forward (90°) and back scattering (270°) amplitudes are the same. A plot of the maximum amplitudes as a function of scattering direction shows that there is a systematic difference in the two results, with the ray-Born amplitude about 15% to 20% less than the discrete wavenumber result (Figure 7). An error of ap-

proximately 2% results simply because the volume of the discretized version of the sphere is 98% of the true sphere. The rest of the variation is explained by complicated interactions of the plane wave with the sphere. Because the impulse response of the sphere increases more rapidly with frequency than the amplitude of the incident wavelet decreases for the low frequency source wavelet, the maximum response after convolution is actually shifted to a slightly higher frequency (Gibson, 1991). As the amplitude of Rayleigh scattering goes as ω^2, this increases the amplitude of the discrete wavenumber solution. This is not reflected in the ray-Born solution, since it only includes the ω_0^2 specified for the center frequency of the incident wavelet.

As the incident center frequency increases to 1 Hz and the ratio η_p decreases to 4.5 (Figures 5B, 6B), the two methods compare about as well as for $\eta_p = 18$, noting also the amplitude plot in Figure 7. Errors are less than 20% in all directions for the P-wave amplitudes and less than 10% for all back scattered energy. Decreasing the incident wavelength further, however, causes the results for the ray-Born method to begin to degrade. We see that the spherical harmonic solution predicts that the back scattering amplitude at 270° will become approximately constant for shorter wavelengths although forward scattering amplitude increases significantly with frequency (Figures 5C, 6C). In one sense, the comparison of maximum amplitudes is not a strictly valid measure of equivalence for the higher frequency results in back scattering, since the discrete wavenumber results show that for $\eta_p = 0.9$ (5 Hz), both shear and compressional wave back scattering have the form of two reflections from the front and back of the sphere, while the ray-Born method yields only a single wide pulse due to insufficient cancellation of back scattered waves. Therefore, comparing the amplitude of the single ray-Born wavelet with the values for the two reflected arrivals from the discrete wavenumber results does not reflect the true mismatch of waveforms. The scattered shear waves were shown by Gibson (1991) to lead to the same conclusions regarding the accuracy of the ray-Born method.

It is worth noting, however, that in spite of the limitations of the Born approximation

the results for forward scattering at 90° from both solution methods still tend to compare relatively well at higher frequencies. Also encouraging is that both methods predict a much shorter pulse of higher apparent frequency for forward scattering than for back scattering and that the total width in time of energy at each observation point is the same. The ray-Born method succeeds in matching the gross features of the wavefields, including achieving at least some of the general trends of amplitude variation with respect to both scattering direction and increasing frequency. Details of the reflections are missing from the Born approximation.

We computed the scattered fields using both methods for P and S-wave velocity perturbations of 10% and 50% as well as the 1% perturbation results shown here. The comparisons are essentially the same as these results, although the details of the complete waveform solution change slightly for the 50% velocity perturbation. These are not reproduced by the ray-Born method, which has strictly linear behavior with respect to variation in elastic constants. The amplitude comparisons become only slightly worse as the velocity perturbations increase to 50%. The more significant failures of the ray-Born solution are still caused by increasing frequency. Therefore, we conclude that a principal requirement for accurate solutions using the ray-Born technique with the degrees of heterogeneity we considered is that the incident and scattered wavelengths must be four to five times larger than the length scale of the heterogeneity, a restriction which for the case above corresponds to frequencies less than or equal to 1 Hz. As the magnitude of the perturbations decreases, this requirement can be relaxed as the Born approximation will be more accurate for weaker heterogeneity. Conversely, for equal accuracy for larger perturbations, a somewhat larger ratio of wavelength to heterogeneity dimension must be imposed as the stronger velocity changes reduce the accuracy of the Born approximation. Even when the wavelength ratio is larger than 5, subtle aspects of wave interaction with heterogeneity can degrade results, as for the 0.25 Hz scattering for our spherical model, where the resonances of the sphere cause a shift of the principal response frequency.

These conclusions regarding the accuracy and validity of the ray-Born method are sup-

18

ported by the analysis of Hudson and Heritage (1981). By assuming that the quantities $|\delta\lambda/\lambda^0|$, $|\delta\mu/\mu^0|$, $|\delta\rho/\rho^0|$, $|\frac{2\pi}{\eta}\frac{\delta\lambda}{\lambda}|$, and $|\frac{2\pi}{\eta}\frac{\delta\mu}{\mu}|$ are all small, it was shown that the series solution returns the Born approximation. Therefore, conditions for validity of the Born approximation according to Hudson and Heritage (1981) can be stated as:

$$|\frac{2\pi d}{\lambda_s^0}\frac{\delta\lambda}{\lambda^0}| << 1 \tag{22}$$

and

$$|\frac{2\pi d}{\lambda_s^0}\frac{\delta\mu}{\mu^0}| << 1. \tag{23}$$

Here λ_s^0 is shear wavelength in the background medium. These conditions are very similar to those discussed above regarding results from the comparisons of the more complete numerical solutions with ray-Born results.

Although density perturbations were not considered in the above examples since our applications consider only elastic constant perturbations, the restrictions on accuracy of the ray-Born method should be much the same as for elastic properties. Both types of perturbations occur in convolutional integrals over volume and time of the same form in equation (6). Therefore, the main factor that controls the accuracy of the Born approximation is still the rapidity of variation of the incident wavefield with respect to the volume of the heterogeneity. The only difference is that for density, the particle acceleration multiplies the perturbation, whereas the strain multiplies the elastic constant variation. Both acceleration and strain vary with the same incident wavelength.

SYNTHETIC SEISMOGRAMS FROM A FRACTURE ZONE MODEL

Given the guidelines established in the comparisons with the complete solution for scattering by an elastic sphere, we apply the method to a layered earth model containing a relatively thin but laterally extended zone of fracturing in the subsurface. Using the ray-Born method,

19

we can easily compare the expected seismic response of the model without the fractured region and with isotropic and anisotropic fracturing present. In addition, the effects of various crack filling materials on the back scattered displacement fields are tested.

The background earth model is presented in Figure 8. It consists of three layers overlying a half-space. The source is located at a depth of 0.25 km in the top layer, which is 0.50 km thick, and receivers are located on the free surface at offsets from the source epicenter of 0 to 1.95 km at an interval of 0.05 km, yielding a total of 40 observation points. A simulated fracture zone is located in the third layer, and it is shaped like a rectangular prism with dimensions of 0.315 km, 0.099 km and 0.018 km in the x, y and z directions, respectively. These axis directions are chosen such that the receiver array is contained within the $x - z$ plane (Figure 8). We applied a center frequency of 25 Hz for the source wavelet, and the lattice spacing was set to 0.009 km in all coordinate directions. The shear wavelength is 9.6 times the lattice spacing so that the ray-Born results should be valid for back scattered waves. One end of this heterogeneity is located under the source point, and the region is centered under the receiver array in the y direction, the direction perpendicular to the receiver array. Though the background model is one-dimensional, the ray-Born solution requires three-dimensional calculation of the Green's tensors due to the three-dimensional nature of the scattering lattice. This example allows the paraxial method to be used to full advantage, however, as rays need only be traced down the axis of the lattice in the $x - z$ plane and the paraxial corrections can be used to project the results out of this symmetry plane. Considerable computation time is saved, since the need to trace rays along multiple azimuths is eliminated.

To calculate the scattered field for the isotropically and anisotropically fractured inhomogeneity, we use the perturbations to the Lamé parameters given by the Hudson theory for the effective elastic moduli of a fractured medium (Hudson, 1980, 1981; Crampin, 1984). The effective moduli are given in terms of an expansion to second-order in crack density $\xi = na^3$, where n is the number density of cracks, and a is the radius of the penny-shaped cracks.

20

We applied a crack density of 0.10, and assumed an aspect ratio of 0.005. For the first case, we consider cracks which are dry or, equivalently, filled with gas under low pressure. The Lamé parameters for the unfractured layer and the fractured perturbations are presented in Table 1. For the case of perturbations due only to fine cracks, density variations are not important since the porosity volume is very small.

Shear Wave Scattering

In the ray tracing for the background field, we included P- and S-waves leaving the source in both the upward and downward directions. The reflections from each interface were then modeled, including phases with a single mode conversion from P to S or S to P on reflection, as waves changing mode more than once are generally of very low amplitude. We first consider the effects of the fracture zone on the propagation of SH waves generated by a single force source oriented perpendicular to the receiver line (Figure 9). No compressional waves are emitted in the direction of the receiver array, and all shear signals have a horizontal polarization. Taking the dot product of all the Green s tensors with the source vector then yields a total of only six arrivals for this source on the transverse component, the shear to shear wave reflections from each interface, including the rays reflecting first from the free surface.

The calculated scattered field includes two S to S scattered waves, one leaving the source in the downward direction, and the other reflecting from the free surface and subsequently traveling to the fractured zone. The background field and total field (the sum of background and scattered waves) for the isotropic fracture zone are compared in Figure 10 for the time interval noted in Figure 9. Like the case of reflection from a planar interface, the incident SH-waves do not yield a scattered P-wave signal and only a transverse component of displacement is generated. The total displacement field distinctly shows the presence of the fractured zone. Arrows in Figure 10 mark the arrival times of the two scattered signals on the zero offset trace,

21

and they are clearly of comparable amplitude to the standard reflections from the nearby planar interfaces. The finite extent of the fracture zone can be inferred from the fact that the back scattered waves are only observed in the shorter offset receivers. These synthetic results show that even thin fractured regions can be detected with seismic experiments.

Next we consider the case where the experimental configuration is exactly the same as above, except that within the fracture zone, all the fractures are vertical and parallel. In this anisotropic case, the fractured zone is transversely isotropic with a horizontal axis of symmetry. This symmetry direction provides an additional degree of freedom compared to the isotropic case considered above, as the orientation of the fractures relative to the receiver array must be considered. Figures 11A, 11B, and 11C compare the transverse component total displacement fields computed for vertical fractures aligned perpendicular, parallel, and at 45° to the receiver array, respectively. The resulting perturbations to the elastic constants are given in Tables 2, 3 and 4. These constants are different for each case due to the rotation of the anisotropic system as the coordinate system is held fixed in direction. Note that for cracks perpendicular to the receiver array $\delta C_{44} = 0$ (Table 2), which significantly affects the total displacement field due to the SH-wave source. Since the only incident strain component which is not vanishingly small is ϵ_{23}, and the only perturbation in this symmetry system which influences scattering in the Born approximation (equation 7) is δC_{44}, the scattered field will be essentially zero. Accordingly, in Figure 11A, no scattered field is present.

When the fractures are aligned parallel to the receiver array, the perturbations to the elastic constants have the same values as in the previous anisotropic model but are rearranged somewhat due to the rotation of the elastic tensor (Table 3). The polarization of incident SH-waves is now perpendicular to the fracture plane. Therefore, there will be large scattered fields, as the incident ϵ_{23} strain now interacts with a non-zero perturbation (equation 7). These effects are seen in the total field synthetic seismograms for the horizontal point force source (Figure 11B). Comparison to Figure 10B shows that the scattered field for this anisotropic model is even larger than the original results presented for the isotropic

22

case. These results are easily understood intuitively as the incident and scattered waves have polarization perpendicular to all of the thin cracks. Thus the maximum effect is to be expected. This shows the sensitivity of shear waves to fracture alignment.

The results for the models with cracks perpendicular and parallel to the receiver array are special cases in that both contain fractures oriented such that incident SH-wave displacement is polarized in a symmetry direction of the anisotropic fracture zone. In the first case, fractures perpendicular to the array, SH polarization is contained in the symmetry plane. In the second example, the SH-wave is polarized parallel to the symmetry axis. If the fracture orientation is at some arbitrary angle to the receiver line, we would expect the resulting synthetic seismograms to be less simple. This effect is shown by the model where the fractures are oriented at 45° to the array, with perturbations to the elastic constants presented in Table 4.

The transverse component total displacement field from the horizontal point force source is presented in Figure 11C. While this signal is very similar to that observed for the isotropic model (Figure 10B) and for the cracks parallel to the array (Figure 11B), for the first time, the SH-wave source results in a significant radial component synthetic seismogram (Figure 12). In the isotropic case, the perturbations are such that $\delta C_{11} = \delta C_{22} = \delta C_{33} = \delta \lambda + \delta \mu$, $\delta C_{12} = \delta C_{13} = \delta C_{23} = \delta \lambda$, and $\delta C_{44} = \delta C_{55} = \delta C_{66} = \delta \mu$ are the only non-zero perturbations. However, the perturbations for the 45° case clearly have other non-zero perturbations (Table 4), and in addition, the equivalencies which hold in the isotropic model are not all true. The result is a complicated secondary source representation which yields both SH and SV energy from an incident SH-wave (equation 7). The vertical component synthetic seismograms are still essentially zero since the vertically propagating shear waves have almost no vertical components of displacement.

By comparing the results for the different orientations of the vertical cracks with respect to the receiver array (Figures 11 and 12), it is clear that scattered or reflected shear waves from anisotropic fracture zones are highly sensitive to the direction of the displacement

23

polarization relative to the crack orientation. The returning energy from the fracture zone varies in amplitude from a very large signal to vanishingly small, and also shows changes in polarization in intermediate directions.

Compressional Wave Scattering

The utility of shear wave observations in the inference of fracture zone anisotropy is clear. However, it is also of interest to understand the information given by compressional wave experiments since it is often easier to obtain good quality, high frequency P-wave data in practical situations. The effects of the isotropic fracture zone perturbations on P-waves are examined by applying an explosion source to the Green's tensors. Figure 13 presents the resulting background displacement field, which now contains non-zero radial and vertical components. The largest disturbances on the vertical component are P-waves, with a pair of reflections from the first interface observed at 0.2 and 0.32 sec on the zero-offset trace, from the second interface at 0.52 and 0.65 sec, and from the third at 0.77 and 0.9 sec. In addition, some large amplitude shear arrivals are observed at larger offsets. The radial component is weaker at near source offsets since near vertical P-waves have minimal horizontal displacement and shear wave conversions only become significant at larger offsets.

For the gas-filled fracture case, the perturbation to the Lamé parameter $\delta\lambda$ is about 5.5 times greater than the change in rigidity μ (Table 1). We thus expect that the compressional wave scattering will be relatively significant, as a change in λ affects only P-wave scattering (Gibson and Ben-Menahem, 1991). Since the nearly vertically travelling compressional waves have a dominantly vertical displacement, only the vertical component synthetic seismograms for the total displacement field for the explosion source are shown in Figure 14, where the arrival times of the principal scattered waves are marked. The scattered compressional waves are easily observed on the vertical component. These results and the example of the transverse component SH-waves show that both compressional and shear waves are of use

24

in the detection of isotropic, gas-filled fracture zones.

In contrast, the scattering of incident compressional wave energy by anisotropic fracture zones yields almost no information on crack orientation. Figure 15 displays the total field synthetic seismograms for the three models considered for the shear waves, with fractures aligned perpendicular, parallel, and at 45° to the receiver array. Comparison of the results for the three models shows that the predicted synthetic seismograms are essentially the same, and that the properties of the scattered P-waves do not depend on the azimuthal orientation of vertical fracture zones. Mathematically, this can be easily understood as the result of the strains induced by the incident wavefield and the consequent secondary source terms due to elastic constant perturbations appearing in equation (7). The incident P-wave strain, mostly ϵ_{33}, interact principally with the perturbation δC_{33}. Though reduced from the isotropic equivalent $\delta\lambda + 2\delta\mu$ (Table 1), this perturbation is still large enough to generate energy on the vertical component seismograms so that the overall trends displayed by the scattered waves are similar to those for the isotropic fracture zone (Figure 14B), though slightly weaker. However, rotation of the vertical fractures with respect to the receiver array leaves δC_{33} invariant (compare Tables 2, 3 and 4). Therefore, the scattered waves are practically constant with fracture orientation and we see that at least for nearly vertically incident P-waves, no information on fracture orientation is available. The physical interpretation of these predictions is also straightforward, as the displacement of the incident wavefield is vertical and therefore more or less parallel to the crack plane for all orientations of cracks; we should not expect much variation of reflection properties. This also explains the reduced amplitude of the scattered waves from the anisotropic zone (Figure 15) as compared to the isotropic fractures (Figure 14).

APPLICATION TO FIELD DATA

The delineation of fracture zones is of great practical interest in the development of geothermal fields, as the permeability created by the fractures can control the fluid flow in the geothermal systems. To facilitate the development of the Larderello geothermal field in Italy (Figure 16), an extensive geophysical study has been conducted (Batini *et al.*, 1983, 1985a, 1985b, 1985c, 1991). Recently, a VSP experiment was conducted in the Badia 1A well in the Larderello field to attempt to further delineate several possible fracture zones (Batini *et al.*, 1991). Interpretation of the processed data from the VSP experiments and a number of other surface seismic surveys resulted in the suggestion that three reflected events from a subsurface feature below the depth of the well bottom and labeled the "H marker" were due to fracture zones distributed over a depth range of approximately 0.200 km. This model is based on some regional seismic observations. We have used ray-Born synthetic seismograms to test this *a priori* hypothesis and to develop a laterally varying model of fracture density in three fracture zones, which accounts for these arrivals as observed from two VSP surveys.

Background Model

A local three-dimensional seismic survey allowed the development of a fairly detailed model of the principal geological layers in the Badia area (Batini *et al.*, 1991). The principal geological features of the locality are two shallow layers consisting of various sedimentary units overlying a thicker zone of metamorphic rock. The L1 and L markers form the lower interfaces of the first and second sedimentary layers, respectively. P-wave velocities for the model are given in a cross-section in Figure 17, a section in the east-west direction which intersects the position of the Badia 1A well. Contour maps of the depths of the L1, L, and H markers are presented in Figure 18, along with the positions of the Badia 1A well and the two locations for the Vibroseis source. One of the shot points is very close to the well and will be called the zero offset point, and the A shot point is 0.981 km north and slightly east

of the well. These maps clearly demonstrate the three-dimensional nature of this modeling problem.

Data

Due to difficult drilling conditions, the Badia 1A well is highly deviated (Figure 19), so that only vertical geophone components have sufficiently high signal-to-noise ratio to analyze the comparatively weak scattered arrivals. Many of the vertical component data traces were, however, extremely noisy after the first arrival, especially at shallower depths. Therefore, a subset of recorded data was used, with receiver positions indicated in Figure 19. Slightly different depth ranges are covered by the geophones from the zero and A offset experiments.

Data from both shot points are shown in Figure 20 where each trace is normalized to unit amplitude on the first arrival. The signal from the far offset VSP is somewhat noisier, since the first arrival prior to normalization is lower in amplitude due to a greater distance from source to receiver. Therefore, noise is amplified more in the normalization than with the zero-offset traces. For both data sets, however, the downgoing waves are clearly much stronger than any reflected arrivals, which are not visible in these sections. To bring out the upgoing reflected waves, we processed the data using a median filter (Hardage, 1983; Reiter, 1991). The moveout velocity on the filter was set to the opposite of the apparent velocity of the downgoing wave to enhance the reflected P-waves, and the filter was applied across 17 traces. After median filtering, the data were subsequently low-pass filtered with cutoff frequencies of 55 and 85 Hz for the zero and A offset data, respectively. Since the predominant signal strength is at 30 Hz, this should not significantly affect the desired signal in the results. The processed data are displayed in Figure 21 with a time squared gain factor applied, and the zero offset data are magnified by a factor of three compared to the A offset plot. The arrivals from the H marker are indicated on these plots. Considering the difference in gain factors applied to the upgoing data plots, it is clear that the signal observed from

27

the A offset source is much stronger, suggesting a lateral difference in the properties of the H marker.

Modeling Results

The geological model (Figures 17 and 18) clearly demonstrates the three-dimensional structure of the sedimentary and metamorphic layers in the Larderello area. This significantly affects the ray tracing procedures which must illuminate the H marker to calculate the scattered waves, as would be expected. To illustrate this problem, we show the ray paths for a fan of rays traced from both the zero and A offset source positions with azimuthal take-off angle in the north-south direction (Figure 22). The resulting ray paths for both source positions have large distortion in the east-west direction due to the L1 and L interfaces (Figure 18), whereas in a one-dimensional earth model, these rays would be entirely contained in a vertical plane. In particular, we see that for the A offset source the bending of the rays at these interfaces is so large that the rays exit the model before reaching the H marker depth. Therefore, computation of the Green's tensors for the incident wavefield in equation (6) requires that we trace fans of rays like those in Figure 22 over all azimuths. Approximately 2,800 rays were traced from the two source positions. Although the ray tracing is simpler from the receivers to the H marker since the metamorphic layer is homogeneous, even more rays are required since the closer proximity of the receivers to the marker increases the range of take-off angles for the fans of rays over all azimuths. Almost 8,000 rays were traced from each receiver to insure sufficient coverage of the H marker. These points regarding the three-dimensional nature of the wave propagation for this problem emphasize the value of the ray tracing approach, which is a practical and feasible method of solution. A more complete solution might in principle be obtained using a finite-difference method, but the required discretization of the three-dimensional model to adequately represent the different layers and the H marker would be prohibitively time consuming.

28

Since the scattered waveforms are stronger on the A offset data, we began by developing a model which would account for these data. A lattice was set up to conform to the map of the H horizon in Figure 18C, though due to limitations of computer storage, we limited the size of the lattice to 1.20 by 1.20 km. It is more efficient for this modeling of scattering by a thin sheet to actually restrict the lattice points to trace the depth of the sheet rather than specifying a regular three-dimensional Cartesian lattice which would have many zero valued nodes. For the A shot point, the lattice ranged from 0.6 to 1.8 km in the east-west direction, the complete width of the map, but only from 0.5 to 1.7 km in the north-south direction. Similarly, the lattice for the zero offset source ranged from 0.8 to 2.0 in the north-south direction. Utilizing a discretization in the two horizontal directions of 0.020 km, this results in a three-dimensional lattice of 61 by 61 by 1 points mapping the H marker. Other forms of data analysis were unable to specify a thickness for the hypothetical fracture zones, though various estimates ranged from 0.010 to 0.060 km. We therefore set the thickness of the lattice to be 0.020 km. A source pulse for both the zero and A offsets was applied by choosing the waveform recorded as a first arrival on representative traces with good signal-to-noise ratio. Final synthetic seismograms should therefore be directly comparable to the field observations.

By trial and error forward modeling, it was determined that a model consisting of three fractured horizons could account for the observations. This was accomplished by temporarily neglecting amplitude effects and matching only the arrival times of the observed data. The depth and shape of the first of the zones, the H1 event, was left to conform to the map in Figure 18C, since it was obtained by the regional three-dimensional survey. The second and third zones, the H2 and H3 events, were defined to have the same lateral variation as shown in Figure 18C, but deeper by 0.090 and 0.170 km, respectively. Our analysis, therefore, confirms a total thickness of the H marker on the order of 0.200 km. It should be noted that the largest amplitudes of the scattered waves in Figure 21 correspond to the arrivals from the H2 and H3 horizons, in agreement with some other regional observations (Batini *et al.*,

29

1991).

After using these initial stages of modeling to define the depths of the H1, H2 and H3 markers, we developed a model to account for the differing strengths of the recorded scattered waves from the two offsets by considering the regions imaged by the two experiments. In Figure 23, we present contour maps of the total travel time from source to lattice point on the H2 marker and back to the receiver for two pairs of receivers at equivalent well positions. The dot in the interior of each plot indicates the minimum time, which corresponds to the Fermat's principle true travel time for the reflected pulse. The contour interval for these plots was chosen so that each contour outlines a Fresnel zone. Sheriff and Geldart (1982) define the Fresnel zone such that the distance from source to scattering surface is a quarter wavelength larger for the outer edge of the zone than from the inner edge. Using the dominant frequency for these data of 30 Hz and the medium velocity of 5.1 km/sec, this distance corresponds to a travel time difference of 0.0083 sec. Since most of the effect of the scattering surface is from that region enclosed within the first Fresnel zone, these figures allow a simple determination of the region of the H2 marker observed in the two VSP experiments.

Comparison of Figures 23A and 23C for receivers at the shallow region of the data and Figures 23B and 23D from the deep portion shows that the A offset survey is imaging a region of the H marker several hundred meters further to the north than the zero offset shot point, though the imaging point for the deeper A offset receiver (Figure 23D) approaches that for the shallow zero offset receiver (Figure 23A). We developed a model assuming that the velocity variations at these markers are due to fracturing and that there must be some larger velocity perturbations toward the north, toward shot point A. After attempting several models, an isotropic model was developed which satisfactorily explains the data. The crack density in the H1 marker, which is weak in both data sets was set to 0.004 uniformly, whereas for the H2 and H3 markers, crack density was set to 0.14 north of the 1.4 km line. and 0.004 south of this border. Temperature and pressure conditions at the depth of the H marker are very uncertain, but other wells suggest that values of about 300°C and several

hundred bar pressure are appropriate (Batini *et al.*, 1983). Under these conditions, the bulk modulus of the pore filling fluid can probably be roughly estimated as 0.1 GPa (Anderson and Whitcomb, 1973). Table 6 shows the resulting perturbations to Lamé parameters. The synthetic seismograms, processed exactly as were the data, are shown in Figure 24. From these results we infer that our model adequately accounts for most of the seismic properties in the region imaged by the A source. The quality of the fit of the zero offset synthedetic is less satisfactory, however, which is at least in part a consequence of the lower signal to noise ratio for the weak scattered wave in this data set. At least part of the signal, especially from traces 55 to 65, is still relatively well modeled.

Although some observations from other wells suggested that vertical fractures are present in the H marker, the successful match of data and synthetic seismograms, particularly for the A offset data, suggest that a purely isotropic model can account for these seismic observations. The synthetic examples shown above for the explosion source clearly demonstrate that in any case a compressional wave experiment will not yield any information allowing a unique interpretation of the presence of vertical fractures, the only difference from the isotropic case being a weaker reflected wave. We attempted to develop a model for the H marker using the elastic constant perturbations appropriate for vertical fractures, but even a crack density as high as 0.30 yielded a signal for the A offset synthetics, which was far weaker than the observed data. This crack density is already so high that it likely violates the single scattering assumption used in the derivation of the expressions for the effective elastic constants, so we did not test any higher values. Instead, we interpret these results as suggesting that the principal source of the scattered seismic energy is an isotropic velocity change which may have some weak anisotropy superimposed due to vertical fractures. The available data does not allow any further conclusions, and, as shown in the synthetic examples. shear wave observations would be necessary to uniquely determine the presence of anisotropy due to vertical fractures.

DISCUSSION AND CONCLUSIONS

The ray-Born method for the modeling of the effects of small. localized regions of inhomogeneity on seismograms is general and can in principle be applied to fully anisotropic models. Limitations on the ray theoretical aspects of the algorithm result from the well known assumption of high frequency methods, namely, that the wavelength of the propagating signal must be much less than the scale length of the background earth model (Ben-Menahem and Beydoun, 1985). Comparisons of ray-Born solutions with the complete. discrete wavenumber solution for the elastic wave scattering from a spherical inhomogeneity illustrate some of the limitations of the Born approximation. The principal restriction is also one of scale lengths. As the ratio of the propagating wavelength to the scale length of the inhomogeneity decreases below a value of about 5, the Born approximation fails to reproduce some significant features of the scattered waves. For the sphere, the missing features were the dual reflections from the front and back of the sphere in the back scattering direction (Figures 5 and 6). The ray-Born solution predicted only a single, broad pulse.

With these limitations in mind, we applied the method to synthetic studies of a thin, laterally extended fracture zone in a simple layered earth model (Figure 8). These synthetic results clearly demonstrate that we expect shear waves to provide useful information on the alignment direction of vertical fractures, as the scattered wavefield varies significantly with the polarization direction of the incident shear wave. In particular, if the incident SH-wave is polarized at an angle to the fracture orientation, the scattered wavefield can have significant energy on the radial component. Similar conclusions were reached by Spencer and Chi (1991) in a theoretical examination of vertically incident shear waves on a uniformly fractured layer or half-space. Mueller (1991) showed the correlation of lateral variation of reflection properties of SH and SV waves with fracture intensity in the Austin Chalk located in Central Texas. These effects, especially when combined with the variation of the observations with different incident polarizations, are not likely to be reproduced by realistic

isotropic inhomogeneity in similar earth models.

The synthetic models also show that compressional wave scattering varies little with crack orientation, although we can still use reflected waves to detect fractured regions. A more unique aspect of the P-wave data is its sensitivity to the material filling the cracks. Since perturbations to the isotropic Lamé parameter λ affect only P-wave scattering and the presence of liquid in the cracks decreases $\delta\lambda$ significantly from the gas-filled case, the amplitude of reflected P-waves also decreases dramatically (Gibson, 1991). These ray-Born results reproduce the classic "bright spot" behavior often used to distinguish gas reservoirs from oil reservoirs.

These guidelines help to interpret the VSP data from the Badia 1A well in the Italian Larderello geothermal field. We developed an isotropic model of three fracture zones contributing to the seismic H marker, accounting for observed reflected waves from below the depth of the well. The model implies that fracture density increases northwards and that this would be a good direction for further exploratory drilling in development of the geothermal resources.

There are, however, several ambiguities in the modeling which cannot be removed due to limitations on the available data and which will affect all seismic studies of fractures, especially those using P-wave data. For example, we cannot rule out the presence of aligned, vertical fractures in the H marker since P-wave scattering from a vertically fractured region shows no indication of fracture orientation. Comparison of synthetic models for isotropic and anisotropic fracture zones of equal crack density (e.g., Figures 14 and 15) shows that the amplitude of the observed P-waves should be reduced for the anisotropic model. The large scattered field in the A offset data was not reproducible with realistic anisotropic crack densities, which gives an indirect evidence for non-vertical fractures in this region. An ambiguity in the ray-Born modeling of fracture zones that enters here is the state of the pore fluids. We applied a value for bulk modulus of the fluid based on some values representative for the estimated *in situ* conditions. It is possible, however, that there is some error in the

33

bulk modulus value. If it is significantly overestimated, the effects of the fractures will be more like those of the synthetic gas-filled fracture models with non-zero bulk modulus of pore fluid and P-wave scattering amplitudes will increase for a given crack density. This might make it possible to develop an anisotropic model accounting for the field data.

Another area of ambiguity is the equivalent effects of increased fracture zone thickness and increased fracture density. Due to the linearity of the method and our representation of the scattering lattices as only a single unit cell in the vertical direction, a doubling of the thickness of the unit cell results in a doubling of the scattered wavefield (equation 8). The same effect results from a doubling of the perturbations to elastic constants. Our assumed value of 0.020 km for the thickness of the three fractured intervals H1, H2 and H3 is of the same order of size as other estimates (Batini *et al.*, 1991), but could very well be off. At the same time, the successful modeling of the observed data, especially for source offset A, suggests that our model of the zones as a single lattice point in thickness is not far off and that the zones are not too thick.

It is possible that both isotropic heterogeneity and superimposed vertical fracturing are present. In this active geothermal area, ongoing hydrothermal processes will likely cause mineral alteration and the sealing of many fractures (Batini *et al.*, 1983; Batini *et al.*, 1985c). Under these conditions, the properties of the rock across the fractured regions could be altered in such a way that a superposition of anisotropic fracturing and isotropic velocity variations is not unrealistic. An increase in porosity due to pores of large aspect ratio would change density proportionately more the elastic properties and would lead to isotropic scattering of elastic waves. It appears from the modeling of the P-wave data that the velocity variations are not entirely due to vertical fracturing in any case, and an isotropic model can explain the data. The only way to concretely determine the presence or absence of anisotropy would be to obtain high quality shear wave data from the same locations.

Similar conclusions regarding the information contained in seismic data were obtained by Stolt and Weglein (1985) in an analysis of multiparameter, linearized inversion methods. Due

to the physics of wave propagation and limitations on observed quantities from experimental configurations, signal-to-noise ratio, and the deep exploration targets, it may only be possible to achieve some knowledge of the location in depth or time of heterogeneity. Increasingly ambitious goals under better conditions or more elaborate experiments include: (1) the sign of the property changes in the heterogeneous zone; (2) the magnitude of the changes; (3) lateral variations of data amplitudes allowing more detailed analysis; (4) inference of multiple physical properties; and (5) true values of all earth properties. Clearly the last goal is only going to be achievable in extremely rare cases. The analysis of the properties of scattered wavefields from fractured zones shows that to achieve anything but the first two or three goals requires very good quality seismic data and must incorporate shear wave observations. Therefore, given that only compressional wave data of relatively low signal to noise ratio was available, the ray-Born method allowed some very useful information on the positions both vertically and laterally of some changes in earth properties.

Our models of both synthetic and field data emphasize the utility of the ray-Born method for modeling scattered wavefields in complicated three-dimensional geological structures. Although there is non-uniqueness in relating amplitude to fracture density and fracture zone thickness, the model for the Badia 1A data does well in predicting the kinematic properties of the scattered waves. It should therefore give concrete and valuable information on the depths of the fracture zones. This type of information is of great utility in geothermal field development. Especially for large three-dimensional problems, the method is a comparatively rapid and efficient means of exploring the effects of different models of small scale heterogeneity within the earth. The results also clearly show the value of shear wave observations in detailed resolution of subsurface seismic properties, particularly for the resolution of anisotropy.

35

ACKNOWLEDGMENTS

REFERENCES

Anderson, D.A.and J.H. Whitcomb, 1973. The dilatancy-diffusion model of earthquake prediction, in *Proceedings of the Conference on Tectonic Problems of the San Andreas Fault System*, R.L. Kovach and A. Nur (eds.), Stanford University Press, Palo Alto, CA, 417–426.

Bamford, D. and K.R. Nunn, 1979. In situ seismic measurements of crack anisotropy in the Carboniferous limestone of Northwest England, *Geophys. Prosp.*, *27*, 322–338.

Batini, F., G. Bertini, G. Gianelli, E. Pandeli, and M. Puxeddu, 1983. Deep structure of the Larderello field: contribution from recent geophysical and geological data. *Mem. Soc. Geol. It.*, *25*, 219–235.

Batini, F., A. Duprat and R. Nicolich, 1985a. Contribution of seismic reflection to the study of geothermal reservoirs in Tuscany (Italy), *Geothermal Resources Council Transactions*, *9*, 245–252.

Batini, F., R. Celati, V. Cigni, P. Squarci, G. Stefani and L. Taffi, 1985b. Development of deep exploration in the geothermal areas of Tuscany, Italy, 1985 International Symposium on Geothermal Energy, Kailua-Kona, Hawaii, Intl. vol., 303–309.

Batini, F., G. Bertini, G. Gianelli, E. Pandeli, M. Puxeddu, and I.M. Villa, 1985c. Deep structure, age and evolution of the Larderello-Travale geothermal field, *Geothermal Resources*

Council Transactions, 9, Part I.

Batini. F., G. Omnes and P. Renoux, 1991. 3-D surface seismic and well seismic applied to the delineation of geothermal reservoirs in metamorphic formations in the Larderello area, Abstr. European Assoc. Explor. Geophys. Annual Meeting, 358–359.

Ben-Menahem, A. and W. Beydoun, 1985. Range of validity of seismic ray and beam methods in general inhomogeneous media—I. General theory. *Geophys. J. R. astr. Soc., 82.* 207–234.

Ben-Menahem, A. and A.G. Sena, 1990. Seismic source theory in stratified anisotropic media, *J. Geophys. Res., 95,* 15395–15427.

Ben-Menahem, A., R.L. Gibson, Jr., and A.G. Sena, 1991. Green's tensor and radiation patterns of point sources in general anisotropic inhomogeneous elastic media, *Geophys. J. Int.*, in press.

Ben-Menahem, A. and S.J. Singh, 1981. *Seismic Waves and Sources*, Springer-Verlag, NY.

Beydoun, W.B. and M. Mendes, 1989. Elastic ray-Born l_2-migration/inversion, *Geophys. J., 97,* 151–160.

Budak, B.M. and S.V. Fomin, 1983. *Multiple Integrals, Field Theory and Series*, Mir Publications, Moscow.

Carswell, A. and W.M. Moon, 1989. Application of multioffset vertical seismic profiling in fracture mapping, *Geophys., 54,* 737–746.

Červený, V., 1985. The application of ray tracing to the propagation of shear waves in complex media, in *Seismic Shear Waves, Part A: Theory*, G.P. Dohr (eds), in *Handbook of Geophysical Exploration*, Section 1: Seismic exploration, *15A*, Helbig, K. and S Treitel (eds.), Geophysical Press.

Červený, V., J. Pleinerová, L. Klimeš, and I. Pšenčík, 1987. High-frequency radiation from earthquake sources in laterally varying structures, *Geophys. J. R. astr. Soc., 88,* 43–79.

Crampin, S., 1978. Seismic wave propagation through a cracked solid: polarization as a possible dilatancy diagnostic. *Geophys. J. R. astr. Soc., 53,* 467–496.

Crampin, S., 1981. A review of wave motion in anisotropic and cracked elastic media. *Wave Motion, 3*, 343–391.

Crampin, S., 1984. Effective anisotropic elastic constants for wave propagation through cracked solids, *Geophys. J. R. astr. Soc., 76*, 135–145.

Crampin, S. and R. McGonigle, 1985. The variation of delays in stress-induced anisotropic polarization anomalies, *Geophys. J. R. astr. Soc., 64*, 115–131.

Crampin, S., R. McGonigle and M. Ando, 1986. Extensive-dilatancy anisotropy beneath Mt. Hood, Oregon and the effect of aspect ratio on seismic velocities through aligned cracks. *J. Geophys. Res., 91*, 12703–12710.

Ensley, R.A., 1984. Comparison of P and S wave seismic data: a new method for detecting gas reservoirs, *Geophys., 49*, 1420–1431.

Evans, K.F., T. Engelder, and R.A. Plumb, 1989. Appalachian stress study, 1. A detailed description of in situ stress variations in Devonian shales of the Appalachian Plateau, *J. Geophys. Res., 94*, 7129–7154.

Gibson, Jr., R.L., 1991. Elastic wave propagation and scattering in anisotropic fractured media, Ph.D. Thesis, Massachusetts Institute of Technology, Cambridge, MA.

Gibson, Jr., R.L. and A. Ben-Menahem, 1991. Elastic wave scattering by anisotropic obstacles, *J. Geophys. Res.*, in press.

Green, A.G. and J. A. Mair, 1983. Subhorizontal fractures in a granitic pluton: their detection and implications for radioactive waste disposal, *Geophys., 48*, 1428–1449.

Gubernatis, J.E., E. Domany, J.A. Krumhansl, R.M. Thompson, 1977. The Born approximation in the theory of the scattering of elastic waves by flaws. *J. Appl. Phys., 48*, 2812–2819.

Hardage, B.A., 1983. *Vertical Seismic Profiling. Part A: Principles.* Geophysical Press, London.

Hickman, S.H., M.D. Zoback, and J.H. Healy, 1988. Continuation of a deep borehole stress measurement profile near the San Andreas Fault, 1. Hydraulic fracturing stress measure-

ments at Hi Vista, Mojave Desert, California, *J. Geophys. Res.*, *93*, 15183–15195.

Hudson, J.A., 1980. Overall properties of a cracked solid, *Math. Proc. Camb. Phil. Soc.*, *88*, 371–384.

Hudson. J.A., 1981. Wave speeds and attenuation of elastic waves in material containing cracks, *Geophys. J. R. astr. Soc.*, *64*, 133–150.

Hudson, J.A. and J.R. Heritage, 1981. The use of the Born approximation in seismic scattering problems, *Geophys. J.R. astr. Soc.*, *66*, 221–240.

Jamison, D.B. and N.G.W. Cook, 1980. Note on measured values for the state of stress in the Earth's crust, *J. Geophys. Res.*, *85*, 1833–1838.

Juhlin, C., J. Lindgren, and G. Collini, 1991. Interpretation of seismic reflection and borehole data from Precambrian rocks in the Dala Sandstone area, central Sweden, *First Break*, *9*, 24–36.

Leary, P.C. and T.L. Henyey, 1985. Anisotropy and fracture zones about a geothermal well from P-wave velocity profiles, *Geophys.*, *50*, 25–36.

Leary, P.C., Y.-G. Li and K. Aki, 1987. Observation and modeling of fault-zone fracture seismic anisotropy—I. P, SV, SH travel times, *Geophys. J. R. astr. Soc.*, *91*, 461–484.

Mandal, B. and M.N. Toksöz, 1990. Computation of complete waveforms in general anisotropic media—results from an explosion source in an anisotropic medium, *Geophys. J. Int.*, *103*, 33–45.

Mueller, M., 1991. Prediction of lateral variability in fracture intensity using multicomponent shear wave surface seismic as a precursor to horizontal drilling in the Austin Chalk, *Geophys. J. Int.*, in press.

Press, W.H., B.P. Flannery, S.A. Teukolsky, and W.T. Vetterling, 1988. *Numerical Recipes in C: The Art of Scientific Computing*, Cambridge University Press, Cambridge.

Reiter, E.C., 1991. Imaging of large offset ocean bottom seismic data, Ph.D. thesis, Massachusetts Institute of Technology, Cambridge, MA.

Sheriff, R.E. and L.P. Geldart, 1982. *Exploration Seismology, Volume 1, History, Theory and*

Data Acquisition, Cambridge University Press, Cambridge.

Spencer, T.W. and H.C. Chi, 1991. Thin-layer fracture density, *Geophys.*, *56*, 833–843.

Stolt, R.H. and A.B. Weglein, 1985. Migration and inversion of seismic data, *Geophys.*, *50*. 2458–2472.

Wu, R.-S. and K. Aki, 1985. Scattering characteristics of elastic waves by an elastic heterogeneity, *Geophys.*, *50*, 585–595.

Ying, C.F. and R. Truell, 1956. Scattering of a plane longitudinal wave by a spherical obstacle in an isotropically elastic solid, *J. Appl. Phys.*, *27*, 1086–1097.

Zoback, M.L. and M. Zoback, 1980. State of stress in the conterminous United States. *J. Geophys. Res.*, *85*, 6113–6156.

Parameter	Background Value (GPa)	Perturbation (GPa)
λ	21.49	-8.34
μ	11.86	-1.49

Table 1. Background Lamé parameters and perturbations for the fracture zone in the model in Fig. 8 with randomly oriented. gas-filled fractures.

Parameter	Background Value (GPa)	Perturbation (GPa)
C_{11}	45.21	-18.6
$C_{22} = C_{33}$	45.21	-4.19
C_{23}	21.49	-4.19
$C_{13} = C_{12}$	21.49	-8.80
C_{44}	11.86	0.0
$C_{55} = C_{66}$	11.86	-2.29

Table 2. Background elastic constants and perturbations for the fracture zone in the model in Fig. 8 with gas-filled vertical fractures oriented perpendicular to the receiver array. The parameters C_{11}, C_{22}, and C_{33} are all equivalent to $\lambda + 2\mu$ in an isotropic medium. while $C_{12} = C_{13} = C_{23} = \lambda$ and $C_{44} = C_{55} = C_{66} = \mu$.

Parameter	Background Value (GPa)	Perturbation (GPa)
$C_{11} = C_{33}$	45.21	-4.19
C_{22}	45.21	-18.6
C_{13}	21.49	-4.19
$C_{23} = C_{12}$	21.49	-8.80
C_{55}	11.86	0.0
$C_{44} = C_{66}$	11.86	-2.29

Table 3. Background elastic constants and perturbations for the fracture zone in the model in Fig. 8 with gas-filled vertical fractures oriented parallel to the receiver array.

Parameter	Background Value (GPa)	Perturbation (GPa)
$C_{11} = C_{22}$	45.21	-12.4
C_{33}	45.21	-4.19
$C_{13} = C_{23}$	21.49	-6.50
C_{12}	21.49	-7.80
$C_{44} = C_{55}$	11.86	-1.15
C_{66}	11.86	-1.29
$C_{16} = C_{26}$	0.0	3.60
C_{36}	0.0	2.31
C_{45}	0.0	1.15

Table 4. Background elastic constants and perturbations for the fracture zone in the model in Fig. 8 with gas-filled vertical fractures oriented at 45° to the receiver array. In an isotropic medium or in a transversely isotropic material in a coordinate system where one of the coordinate axes parallels the axis of symmetry, C_{16}, C_{26}, C_{36}, and C_{45} are all zero.

Crack density	Parameter	Background Value (GPa)	Perturbation (GPa)
$\xi = 0.14$	λ	23.6	-3.33
	μ	23.6	-3.33
$\xi = 0.004$	λ	23.6	-0.10
	μ	23.6	-0.10

Table 5. Background Lamé parameters and perturbations for the fracture zone model for the Badia location H markers. The marker H1 marker was assigned a crack density of 0.004 throughout the model, whereas the computed synthetics applied a crack density of 0.14 to the H2 and H3 markers north of the 1.4 km latitudinal line (Fig. 18).
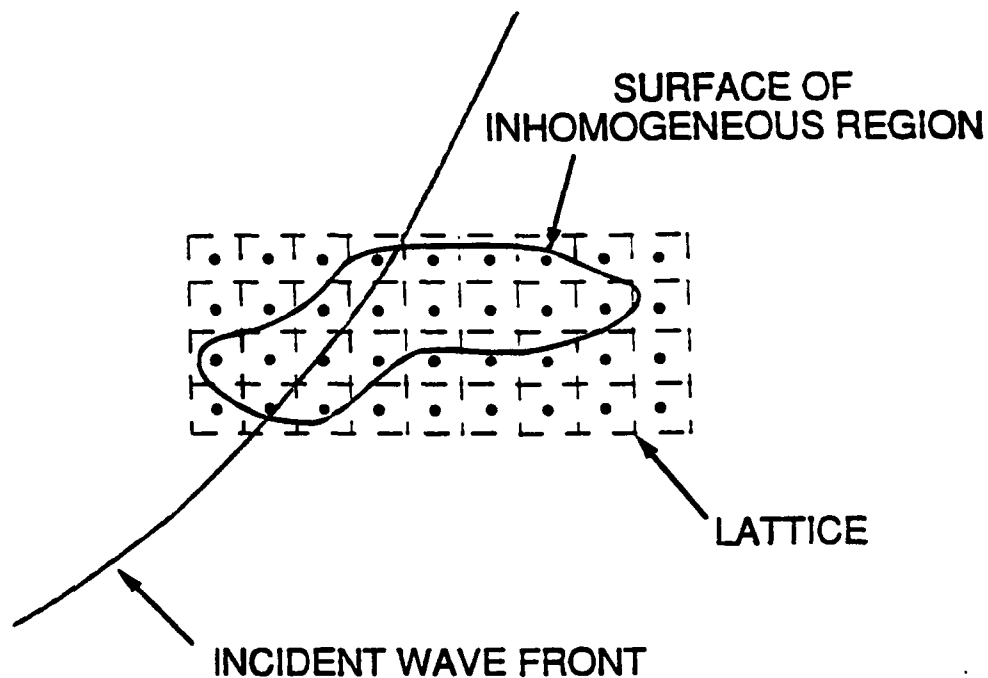
Figure 1: Discretization scheme for implementation of the ray-Born algorithm. A two-dimensional example is shown for clarity, though the actual implementation includes three-dimensional scattering lattices and background models. All lattice points outside the boundary of the inhomogeneity are assigned zero perturbation values, while those points inside the boundary can be assigned non-zero perturbations to density or any of the elastic constants C_{IJ}. As the incident wavefront encounters a lattice point. that particular point becomes a secondary source.

44
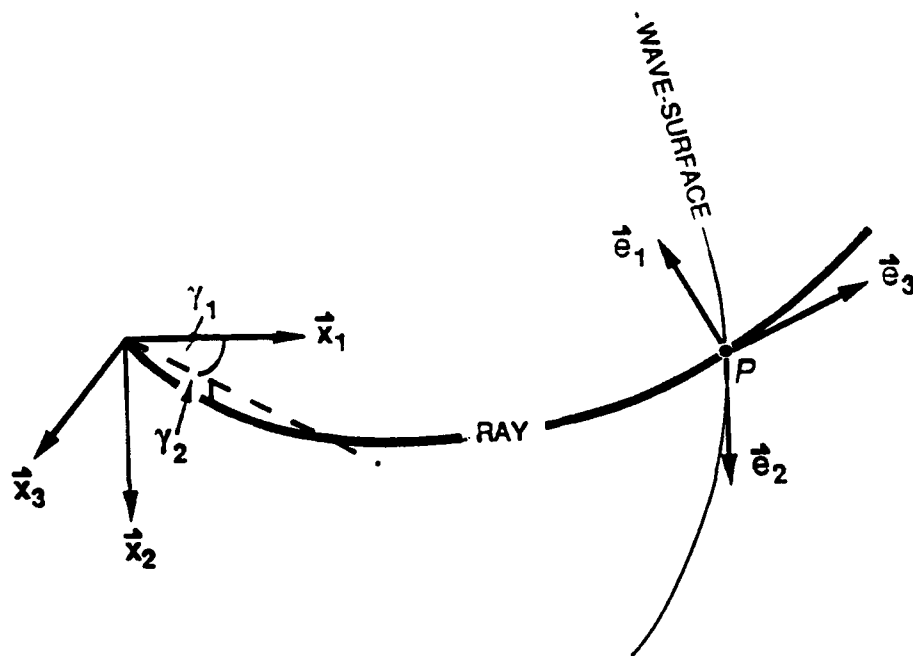
Figure 2: Diagrammatic illustration of the ray coordinates γ_1 and γ_2 and ray-centered coordinate basis vectors e_1, e_2, and e_3. The ray coordinates correspond to the azimuthal and declination take-off angles, γ_1 and γ_2, respectively. At each point P on the ray, the two basis vectors e_1 and e_2 are located in the plane tangent to the wavefront, while the third vector e_3 is tangent to the ray, forming a right-handed coordinate system valid in the vicinity of the ray (Červený, 1985).
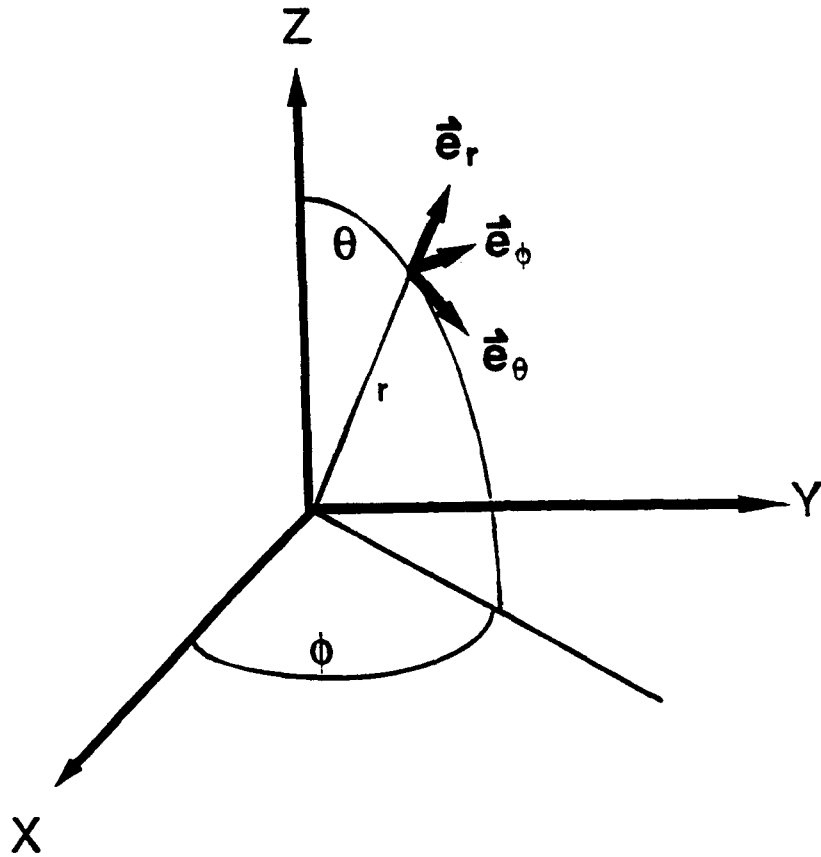
Figure 3: Spherical coordinate system. The scattered wavefields from the elastic sphere are calculated for receiver distances sufficiently distant that the P-wave displacement will be observed entirely on the radial component e_r and the S-wave will appear only on the e_θ component. The shear wave has only a e_θ component due to the symmetry of the problem for a plane P-wave incident along the z axis.

46
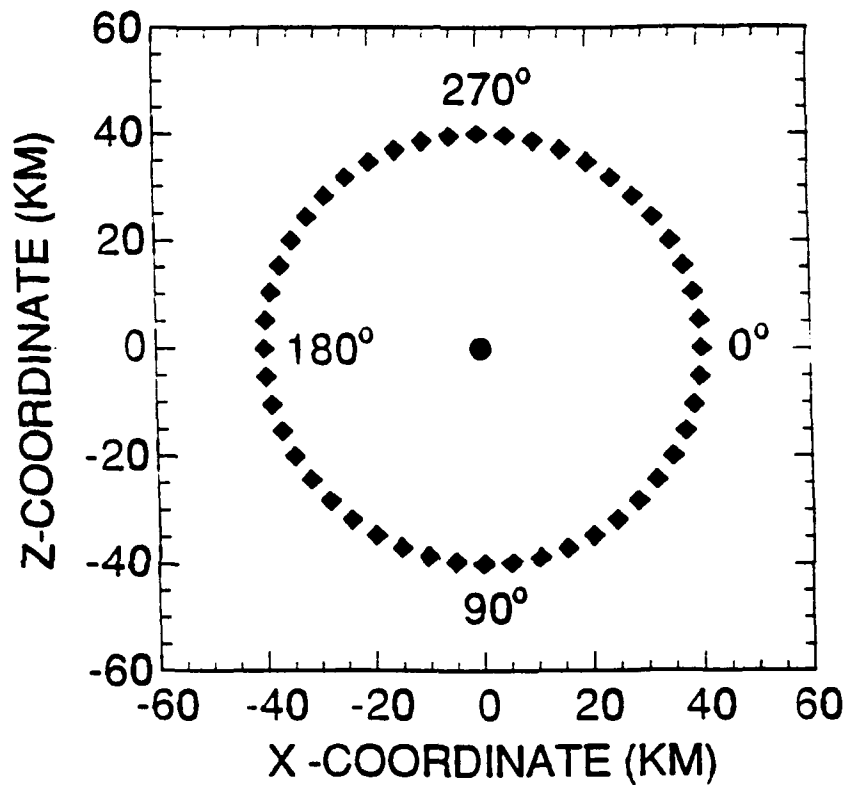
Figure 4: Receiver configuration for the computation of wavefields scattered from an elastic sphere. The sphere is located at the origin of the coordinate system and the incident plane P-wave is propagating in the downwards vertical direction so that the direction 90° corresponds to forward scattering, and 270° is the direction for back scattered waves. The angles given here are equal to the angular coordinate θ in Figure 3 minus 90° and are used for reference in the synthetic seismogram plots.

47
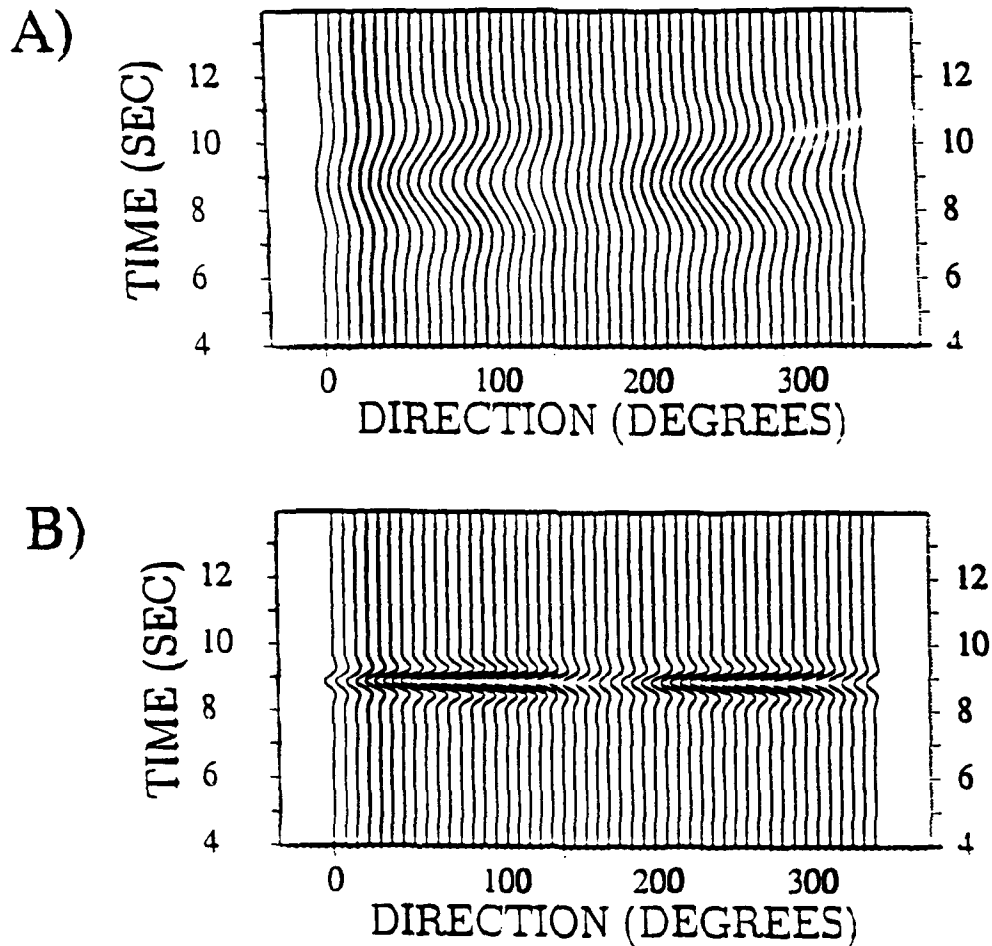
Figures 5A and 5B: ray-Born radial component synthetic seismograms for the scattering from a compressional plane wave vertically incident on a sphere showing scattered compressional waves. Since the amplitudes of the scattered waves increase dramatically with increasing frequency, the scale of the different plots was changed to allow the different waveforms to be observed. A) Ratio of compressional wavelength to sphere diameter $\eta_p = 18$, frequency $f = 0.25$ Hz. B) $\eta_p = 4.5$, $f = 1$ Hz. Plotting scale multiplied by 0.1 relative to the $\eta_p = 18$ plot.

C)

D)
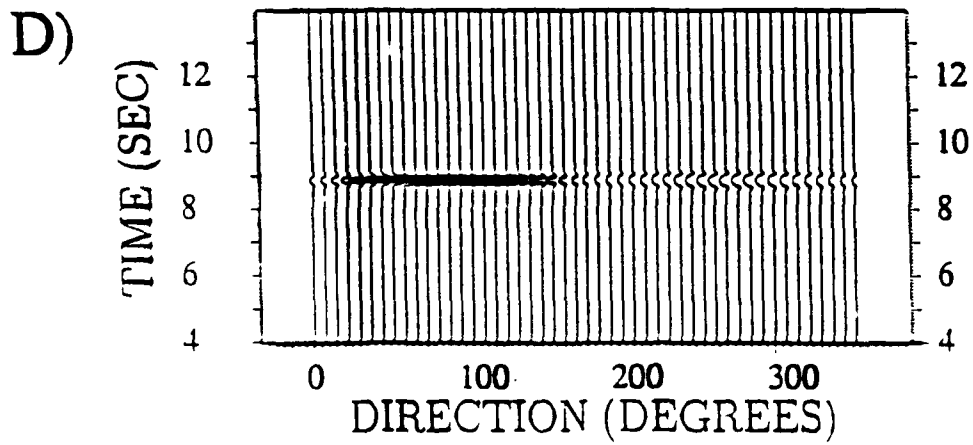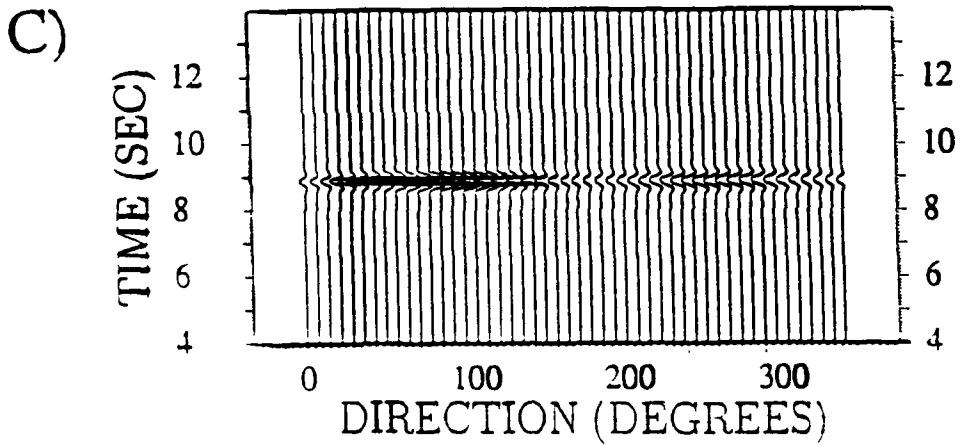
Figures 5C and 5D: C): $\eta_p = 1.8$, $f = 2.5$ Hz. Plotting scale multiplied by 0.02 relative to the $\eta_p = 18$ plot. D) $\eta_p = 0.9$, $f = 5$ Hz. Plotting scale multiplied by 0.01 relative to the $\eta_p = 18$ plot.

49
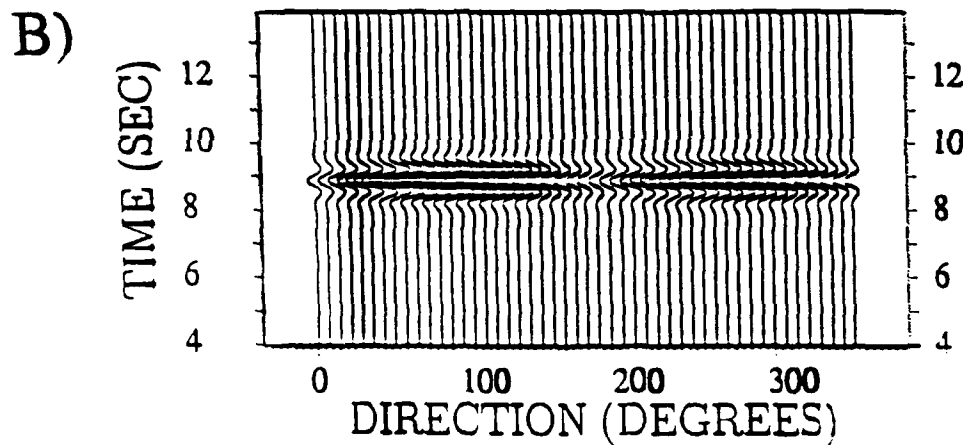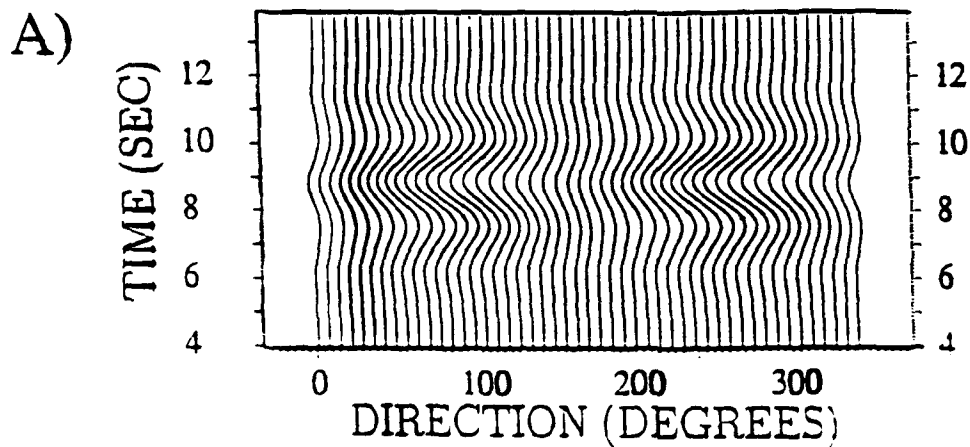
Figures 6A and 6B: Discrete wavenumber radial component synthetic seismograms for the scattering from a compressional plane wave vertically incident on a sphere showing scattered compressional waves. All plot scales for a given frequency are the same as in Figure 5 so that waveforms may be directly compared for the ray-Born and discrete wavenumber methods. A) Ratio of compressional wavelength to sphere diameter $\eta_p = 18$. frequency $f = 0.25$ Hz. B) $\eta_p = 4.5$, $f = 1$ Hz.
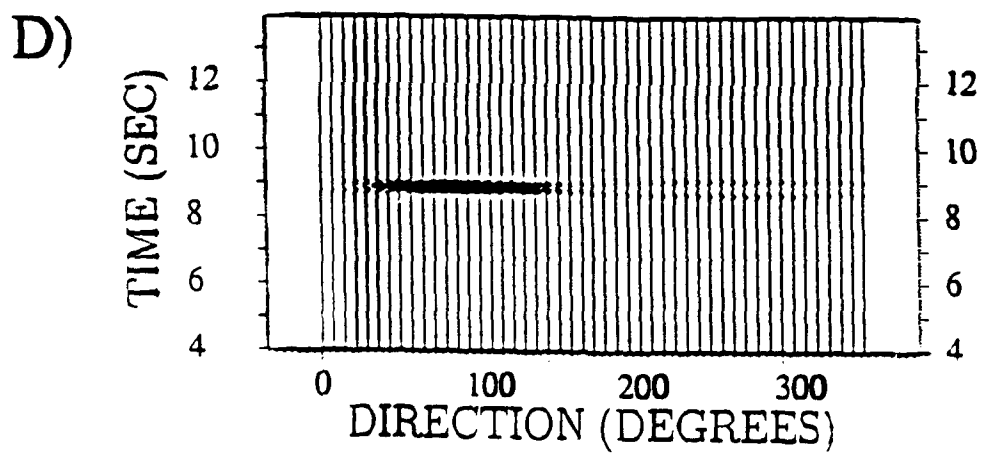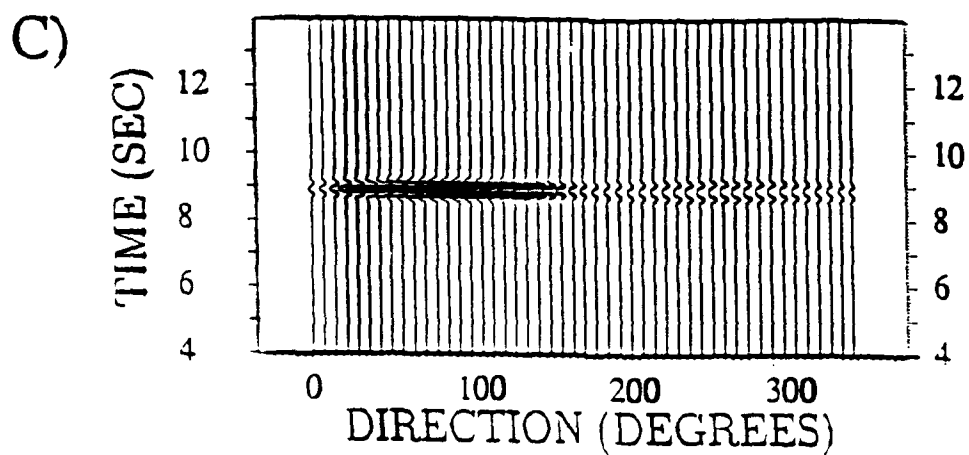
Figures 6C and 6D: C): $\eta_p = 1.8$, $f = 2.5$ Hz. D) $\eta_p = 0.9$, $f = 5$ Hz.

51
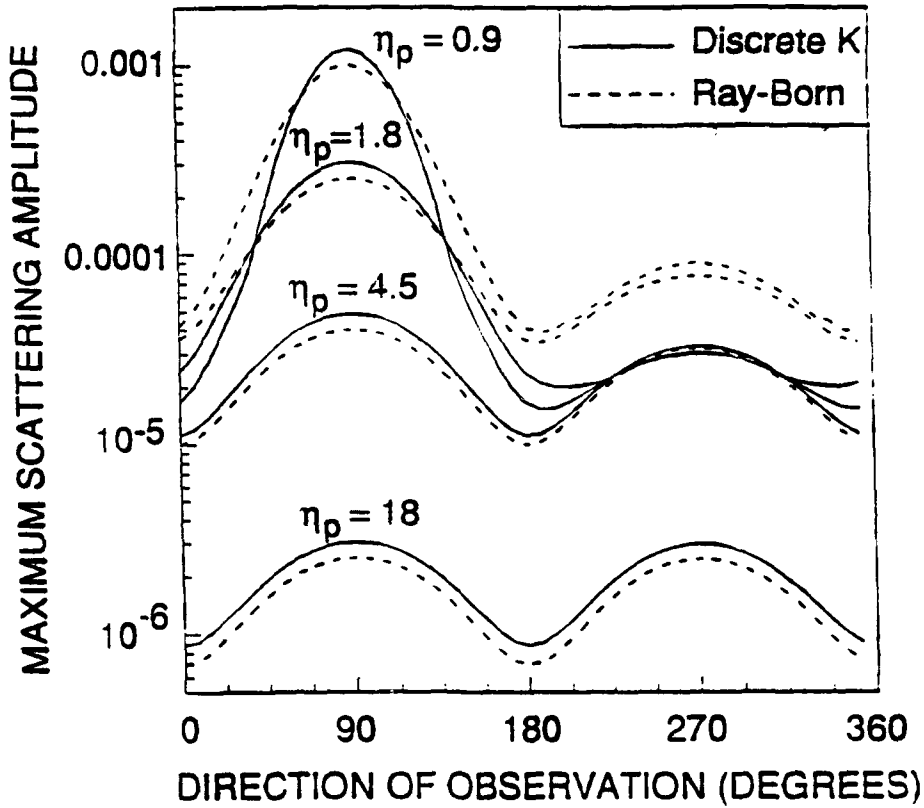
Figure 7: Comparison of the amplitudes of compressional waves scattered from the sphere with 1% velocity perturbations with different values of incident wavelength to sphere diameter ratio η_p indicated. Forward scattering is in the direction $90°$ and back scattering is at $270°$.
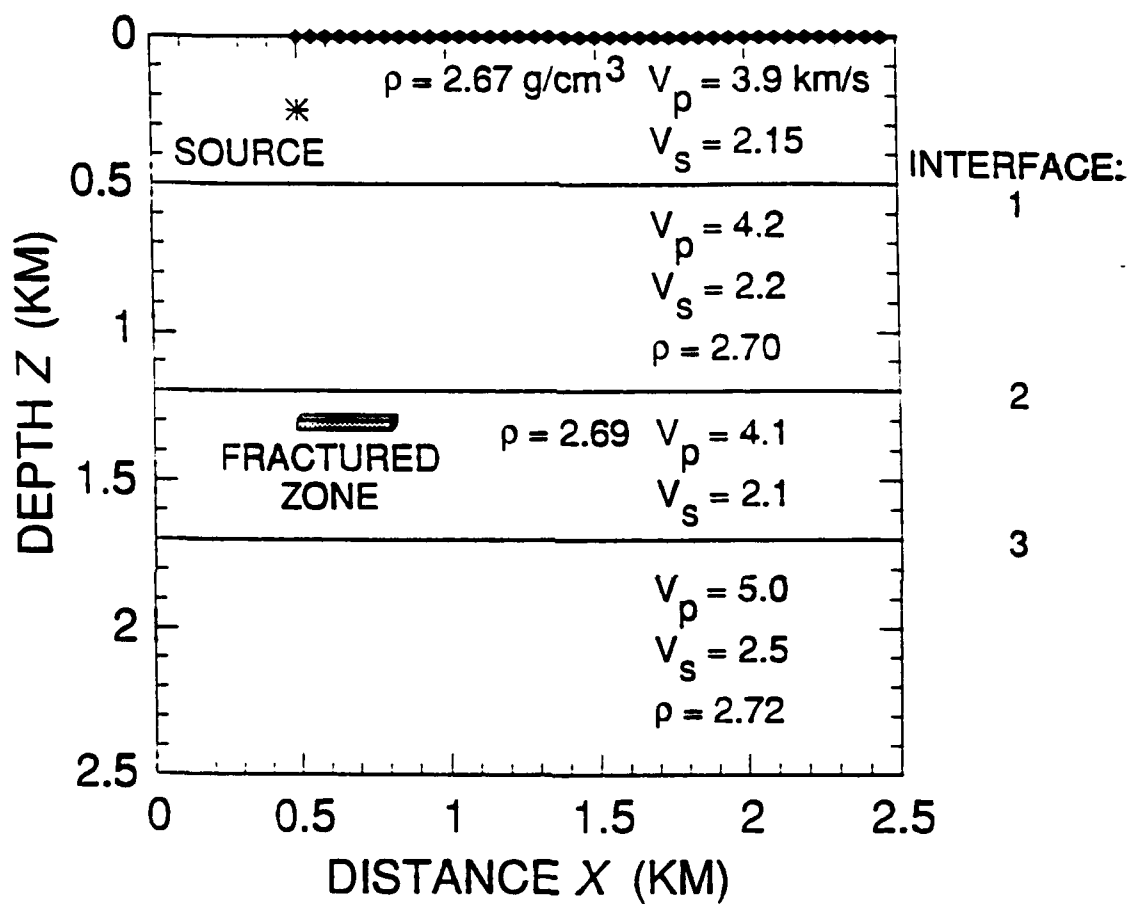
Figure 8: Background model used to calculate synthetic seismograms including the effect of a thin fracture zone. Receivers are indicated by the black diamond symbols, and the position of the source is shown. This model cross-section is contained in the $x - z$ plane, and the y axis is perpendicular to the figure.

53
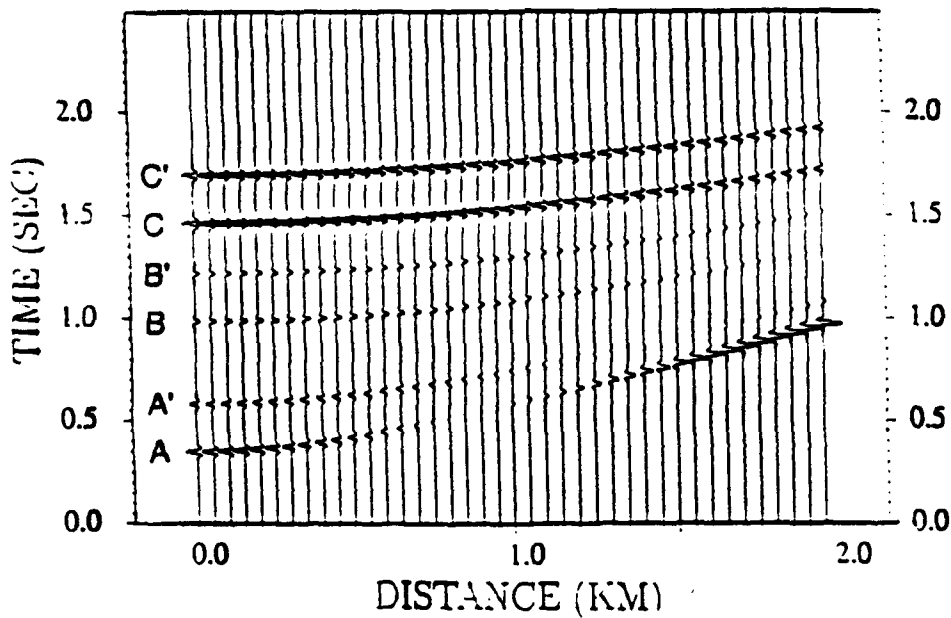
Figure 9: Transverse component background displacement field from a cross-line point source for the earth model shown in Figure 8. Since only SH-waves are radiated in this coordinate plane by the source vector, the radial and vertical component synthetic seismograms contain no signal. Main reflections are identified as follows (prime indicates free surface multiple): (A) S to S reflection from interface 1. (B) S to S reflection from interface 2. (C) S to S reflection from interface 3.
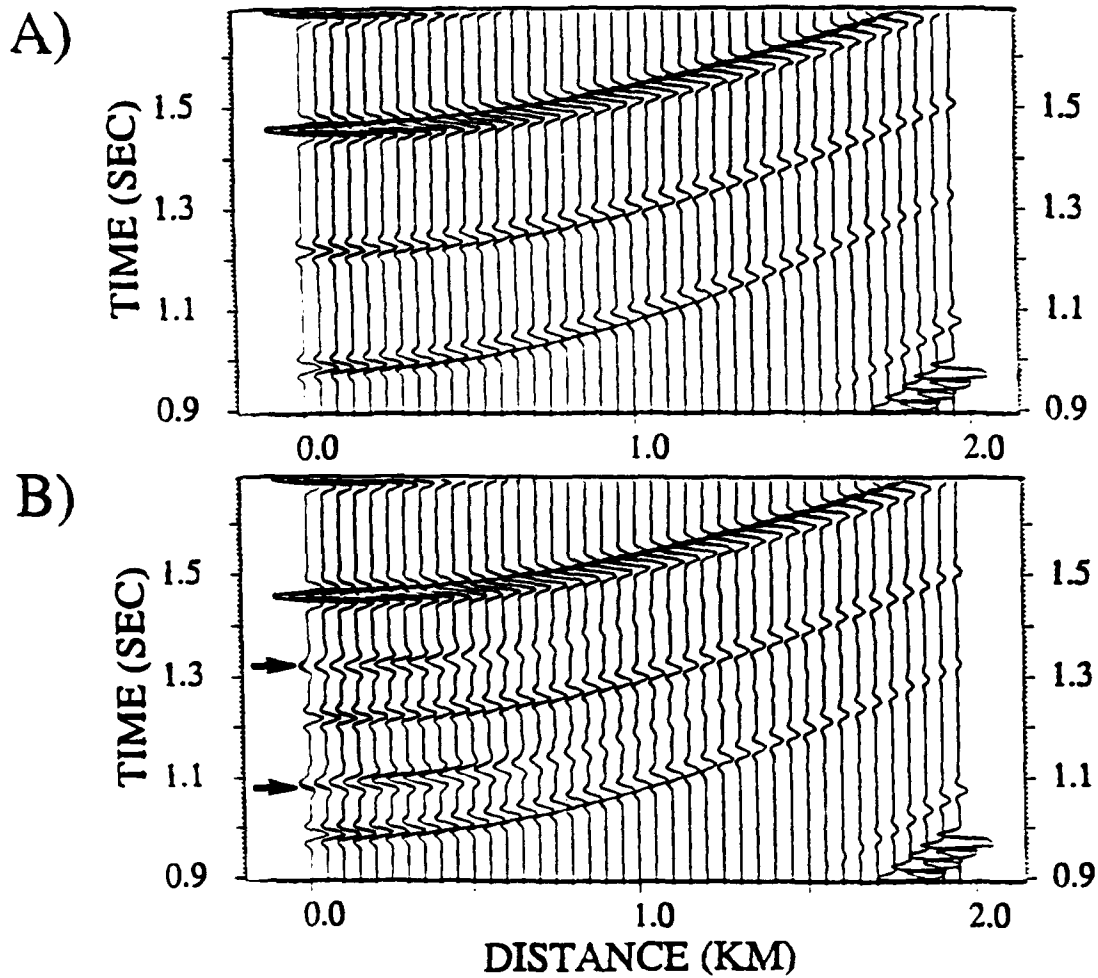
Figure 10: Comparison of the SH-wave transverse component background displacement field and the total displacement field for the model containing an isotropic fracture zone. This figure contains the time window indicated on Figure 9. (A) Background displacement field. (B) Total displacement field.
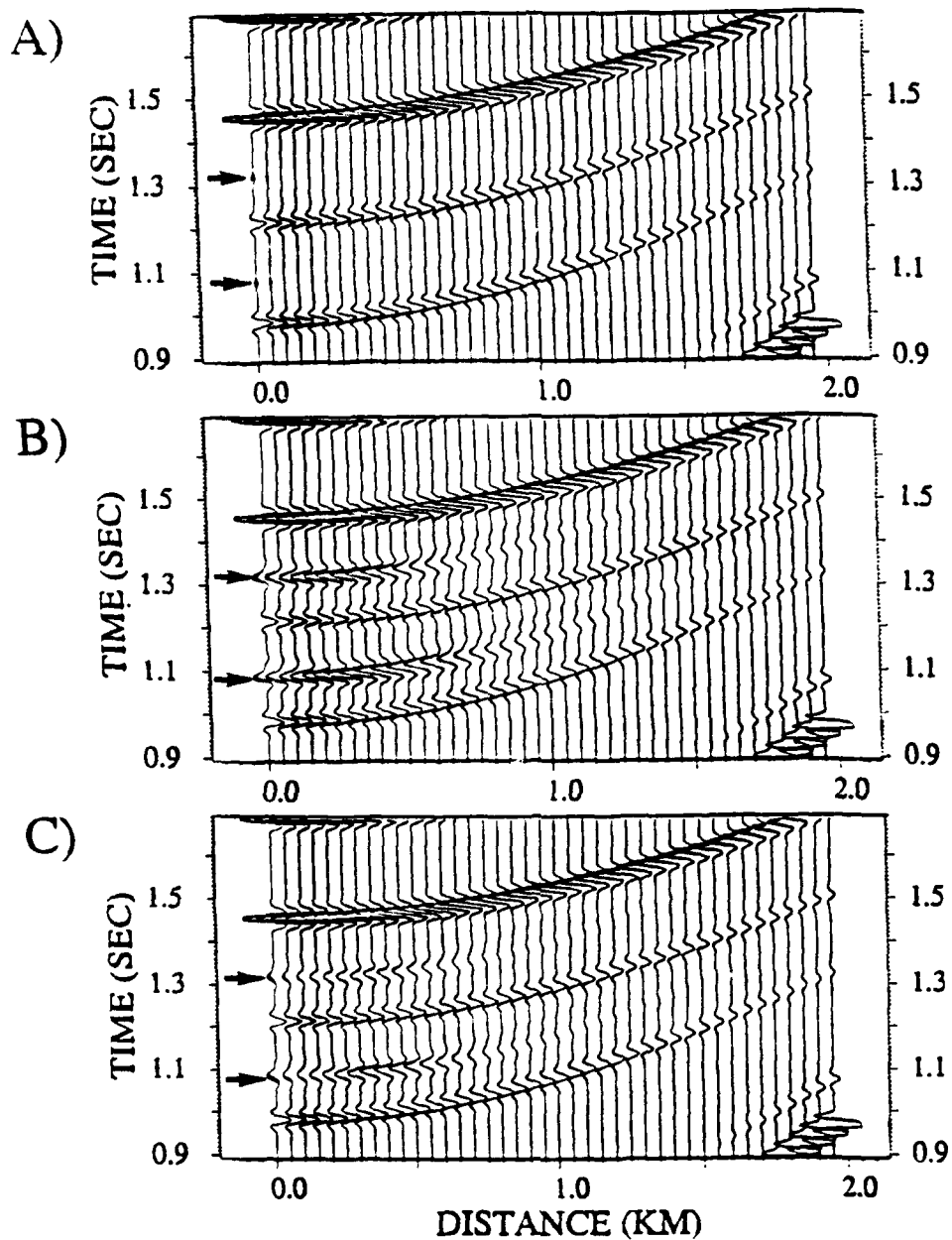
Figure 11: Comparison of the SH wave transverse component total displacement fields for three orientations of the vertical fractures with respect to the receiver array from the model in Figure 8. All plots in this figure are at the same scale as those in Figure 10, and the time window is indicated in Figure 9. (A) Fractures perpendicular to the receiver array. (B) Fractures parallel to the receiver array. (C) Fractures at 45° to the receiver array.
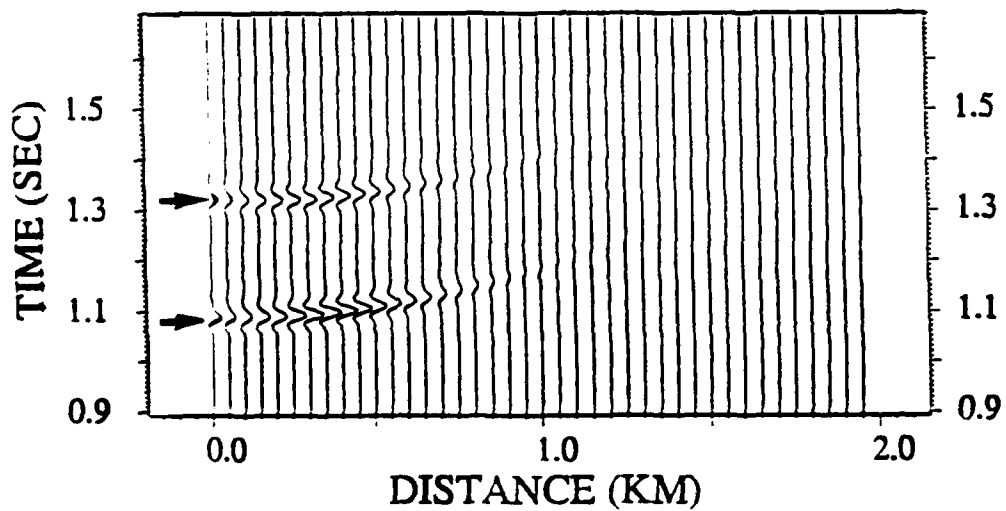
Figure 12: The radial component synthetic total field synthetic seismogram resulting when the anisotropic fractures are aligned at 45° to the receiver array.

57
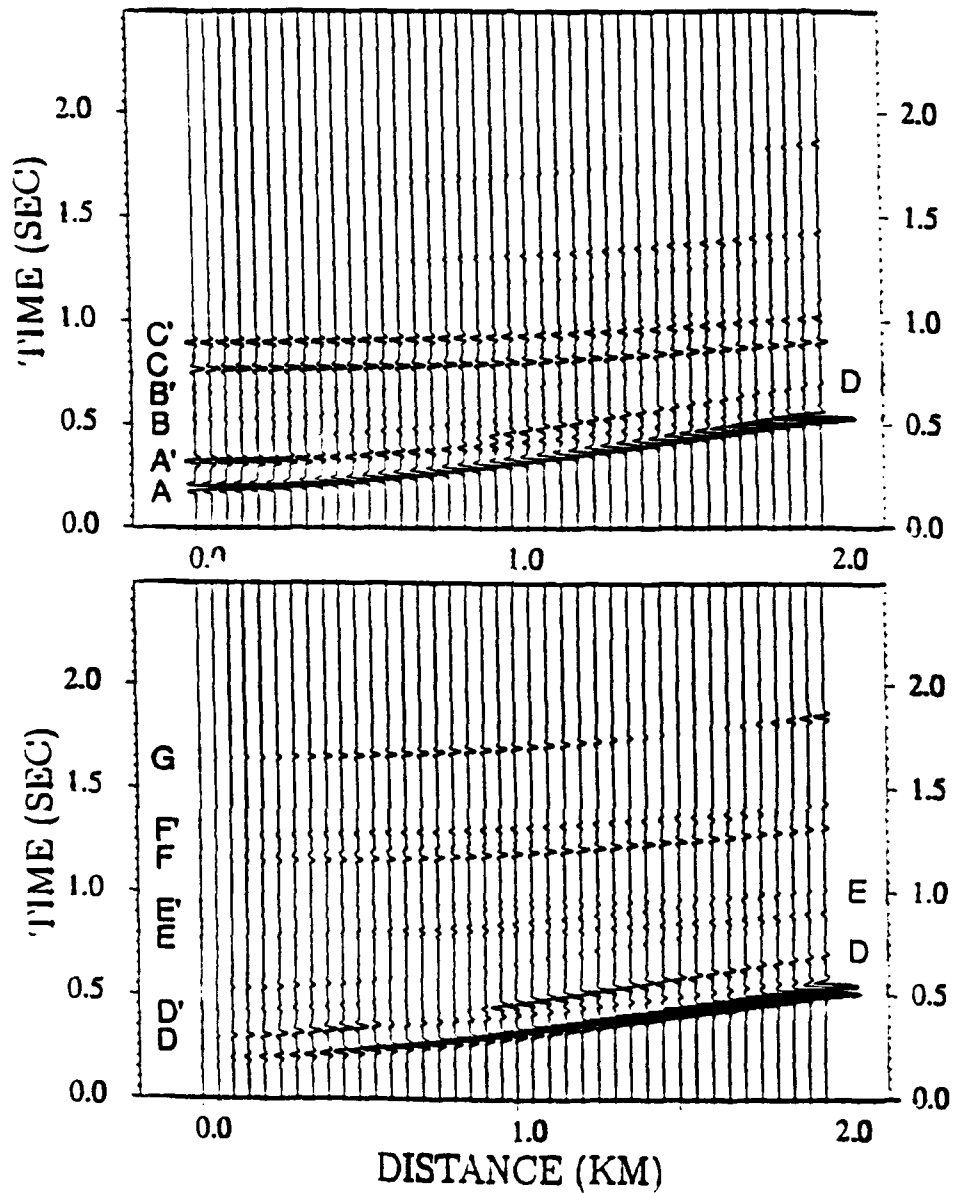
Figure 13: Vertical (above) and radial (below) component synthetic seismograms from an explosion source for the background model in Figure 8. The main reflections are identified as follows (prime indicates a free surface multiple): (A) P to P reflection from interface 1. (B) P to P reflection from interface 2. (C) P to P reflection from interface 3. (D) P to S reflection from interface 1. (E) P to S reflection from interface 2. (F) P to P reflection from interface 3. (G) P to S reflection at free surface, followed by S to S reflection at interface 3.
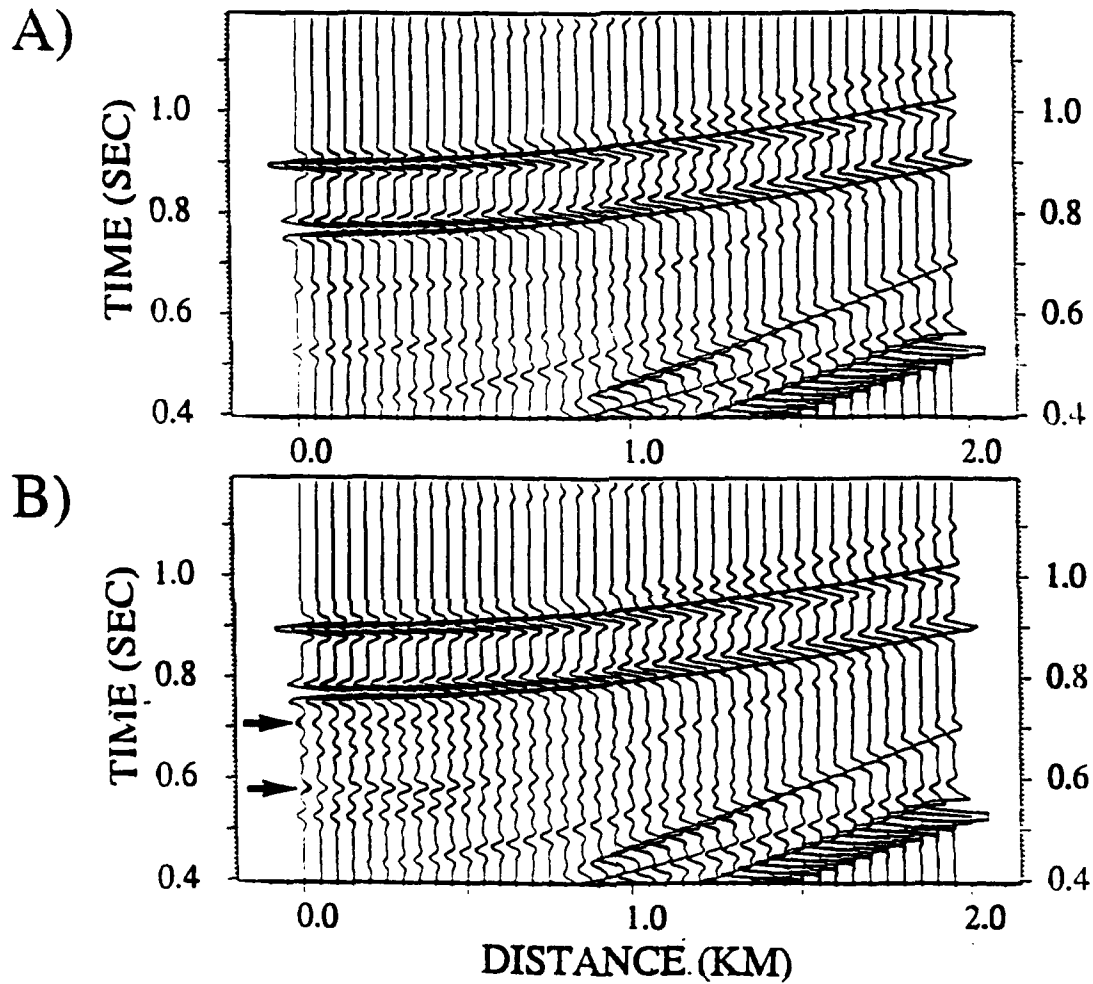
Figure 14: Comparison of the P-wave vertical component background displacement field and total displacement field for the model containing an isotropic fracture zone. This figure contains the time window indicated on Figure 13. (A) Background displacement field. (B) Total displacement field.
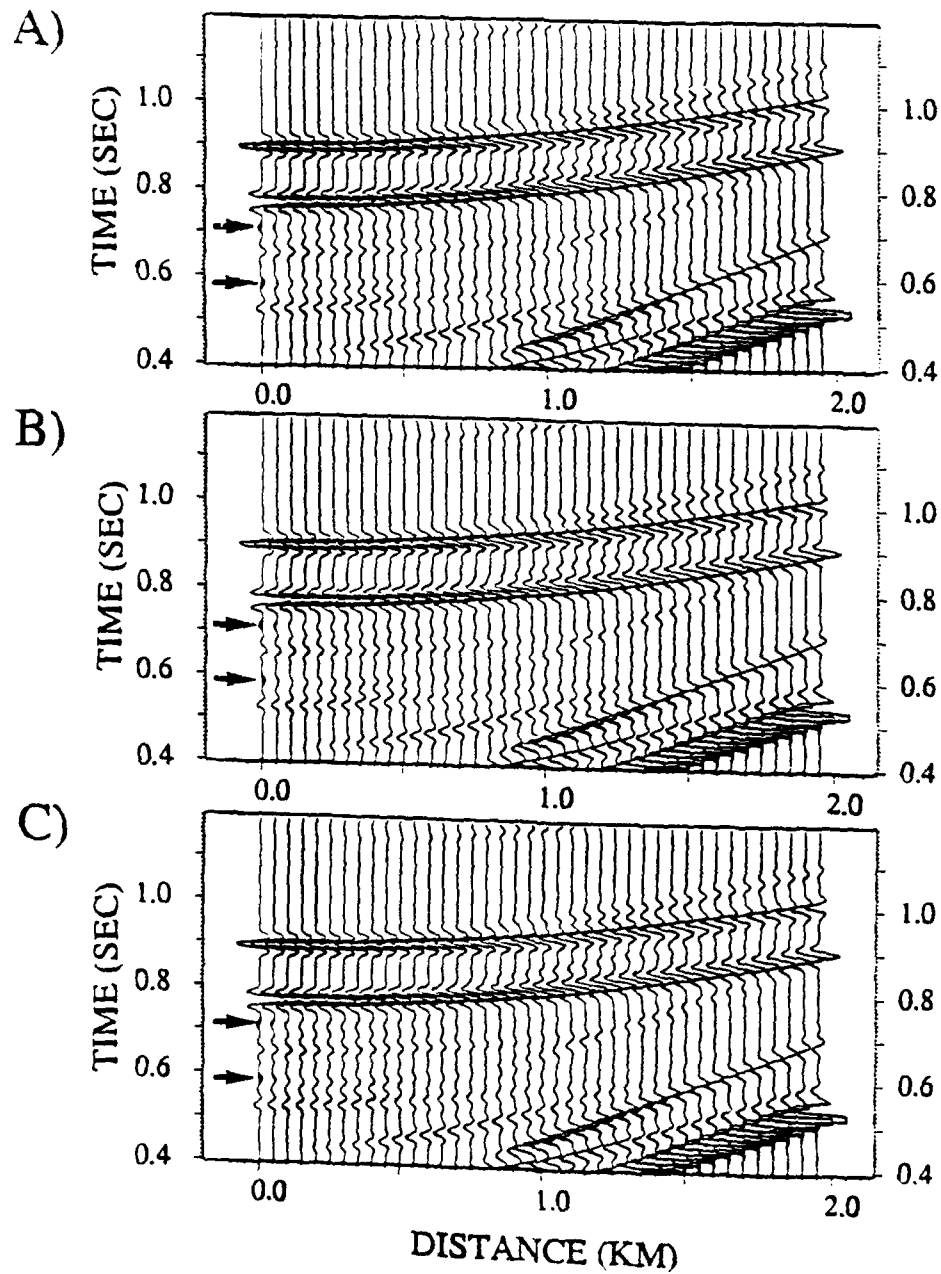
Figure 15: Comparison of the P-wave vertical component synthetic seismograms for three orientations of the anisotropic vertical fractures with respect to the receiver array from the model in Figure 8. All plots in this figure are at the same scale and include the same time window as those in Figure 14. (A) Fractures perpendicular to the receiver array. (B) Fractures parallel to the receiver array. (C) Fractures at 45° to the receiver array.
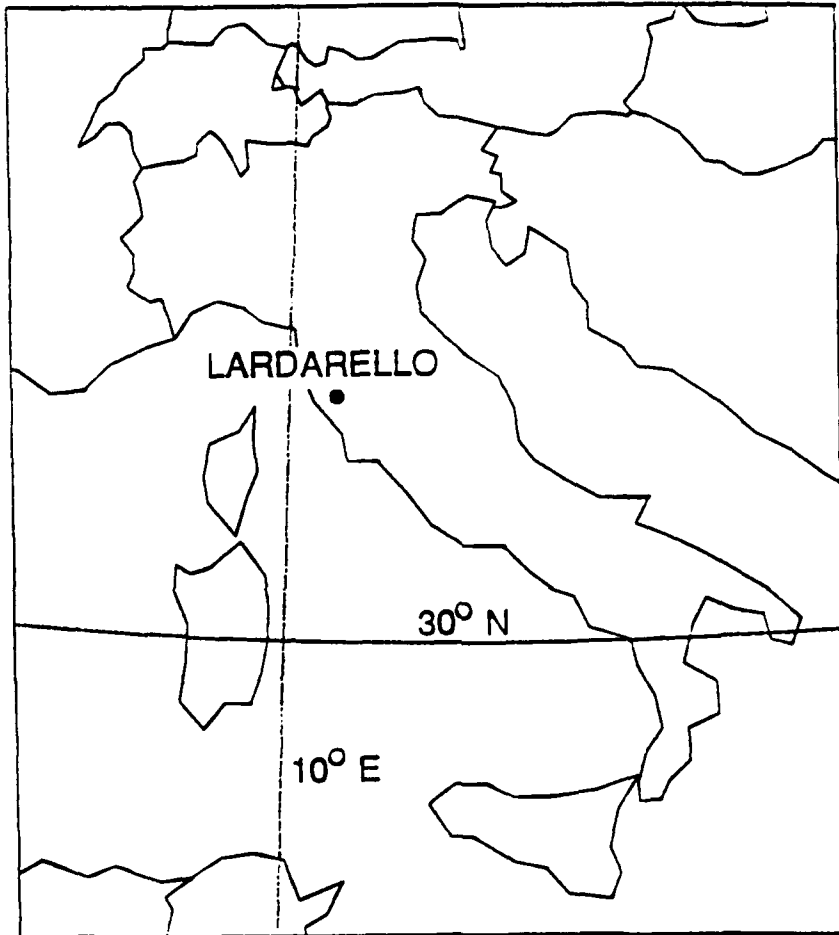
Figure 16: Map showing the location of the Larderello geothermal field in Italy.
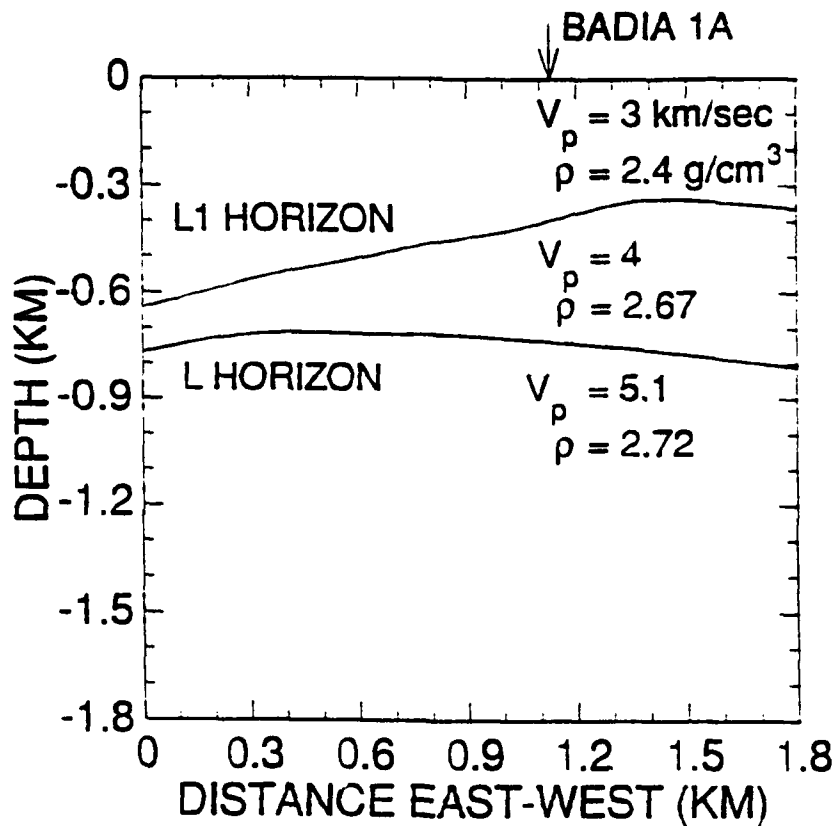
Figure 17: East-west cross-section of the background earth model used to compute the synthetic seismograms for the Badia 1A VSP data. Sedimentary units are present in both layers over the L horizon, while the rock below is metamorphic. The seismic properties of the metamorphic zone are relatively homogeneous so that it may be represented by a single velocity. Compressional wave velocities and densities are indicated in the figure, and shear wave velocities were chosen so that the V_p/V_s ratio was $\sqrt{3}$.
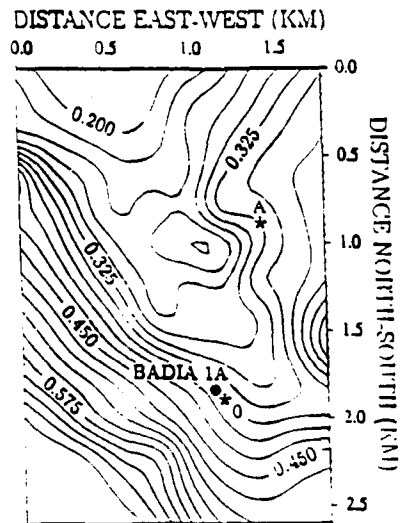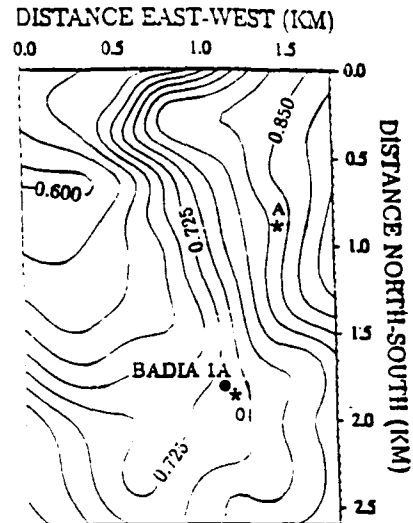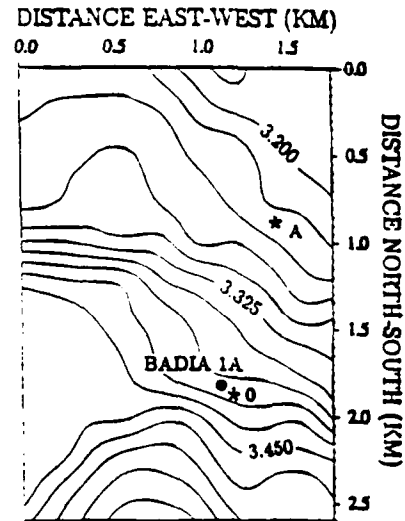
Figure 18: Contour maps of the three surfaces used in the modeling of the Badia 1A VSP data. The positions of the Badia 1A well, the zero offset source position 0 and A offset source position A are all indicated. A) L1 interface. B) L interface. C) H marker.

63
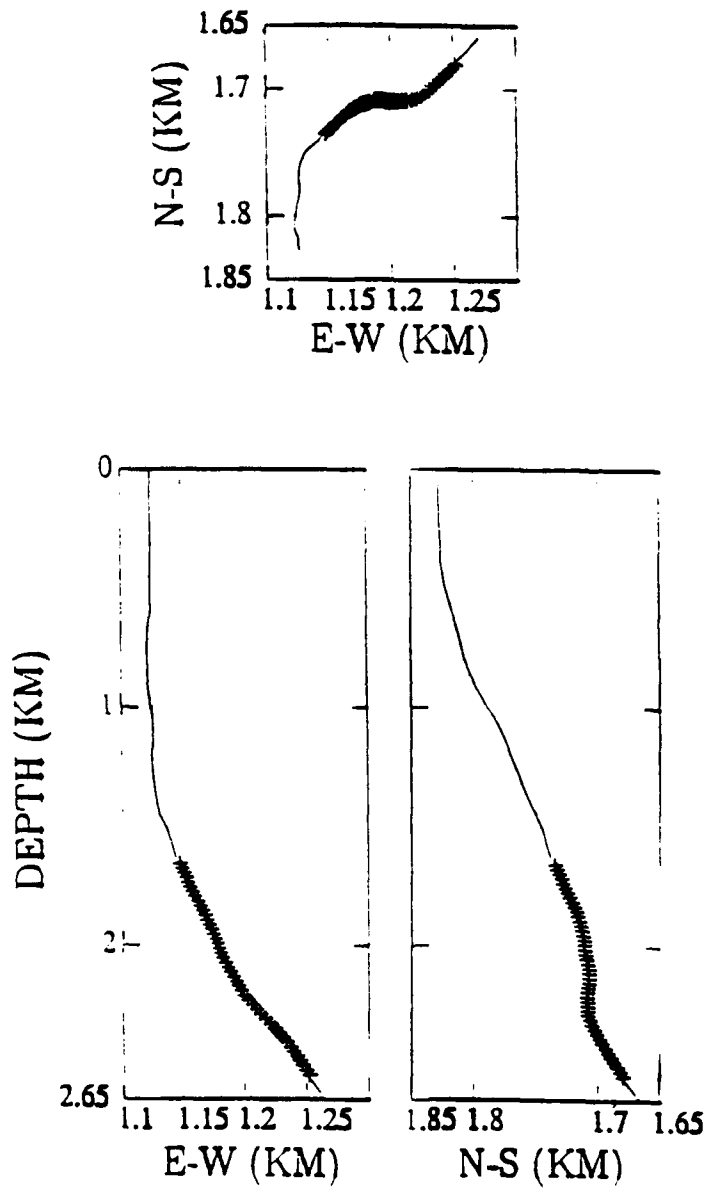
Figure 19A: Positions of geophones and the deviated Badia 1A well. The geophones are plotted in all three coordinate planes. A) Geophone positions for the zero offset source.
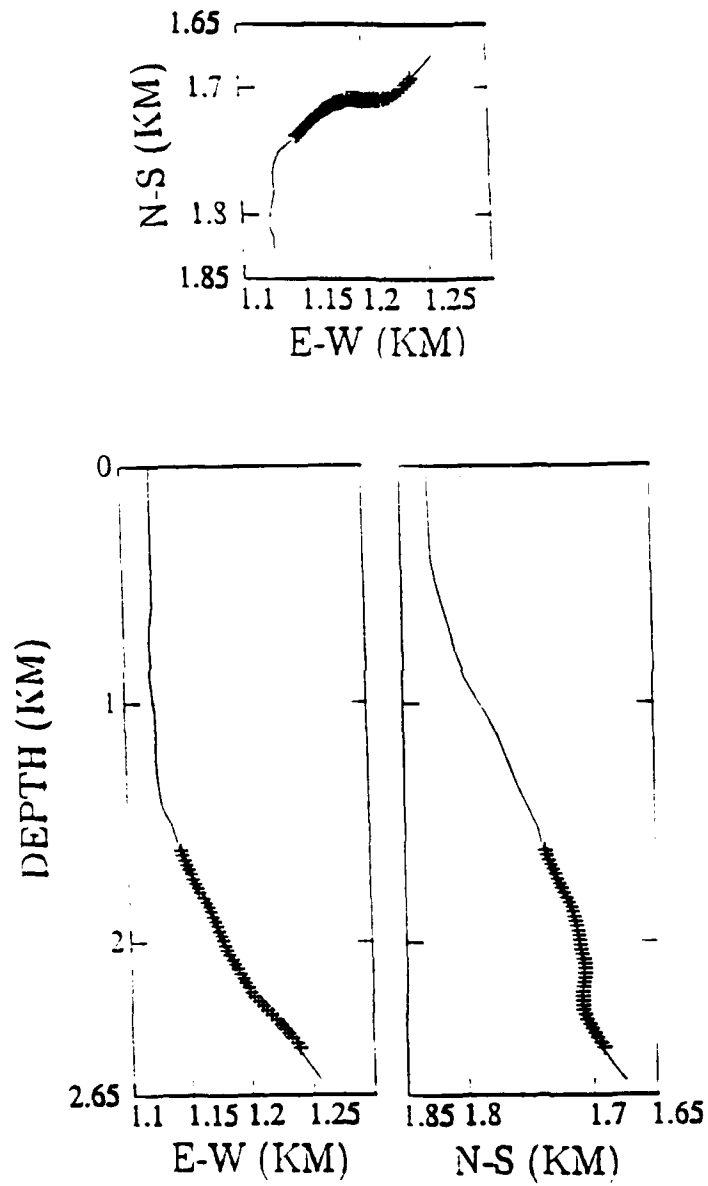
Figure 19B: B) Geophone positions for the A offset source.
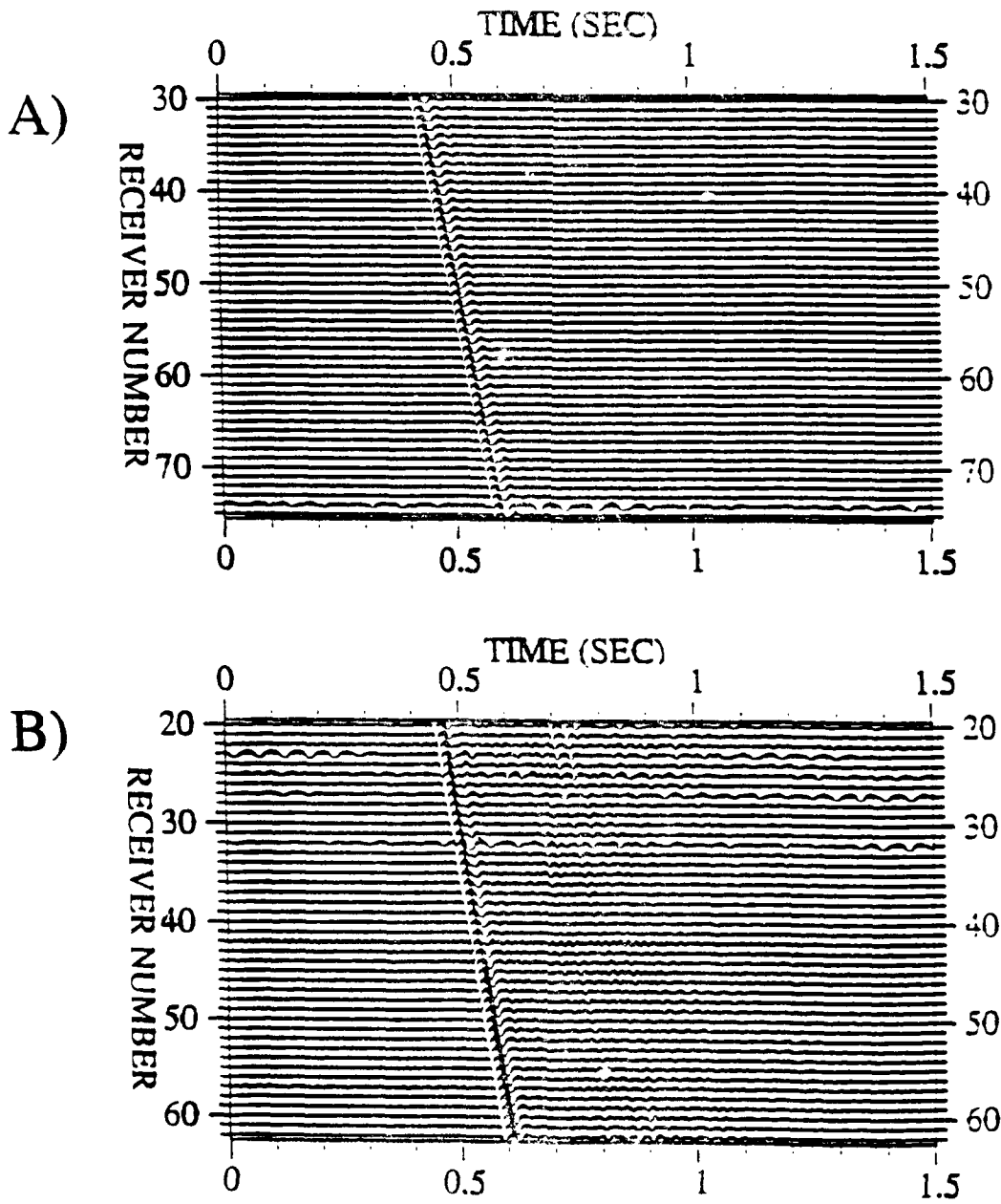
Figure 20: Trace normalized data from the zero offset source (above) and the A offset (below). The data were normalized so that the first arrival had unit amplitude.
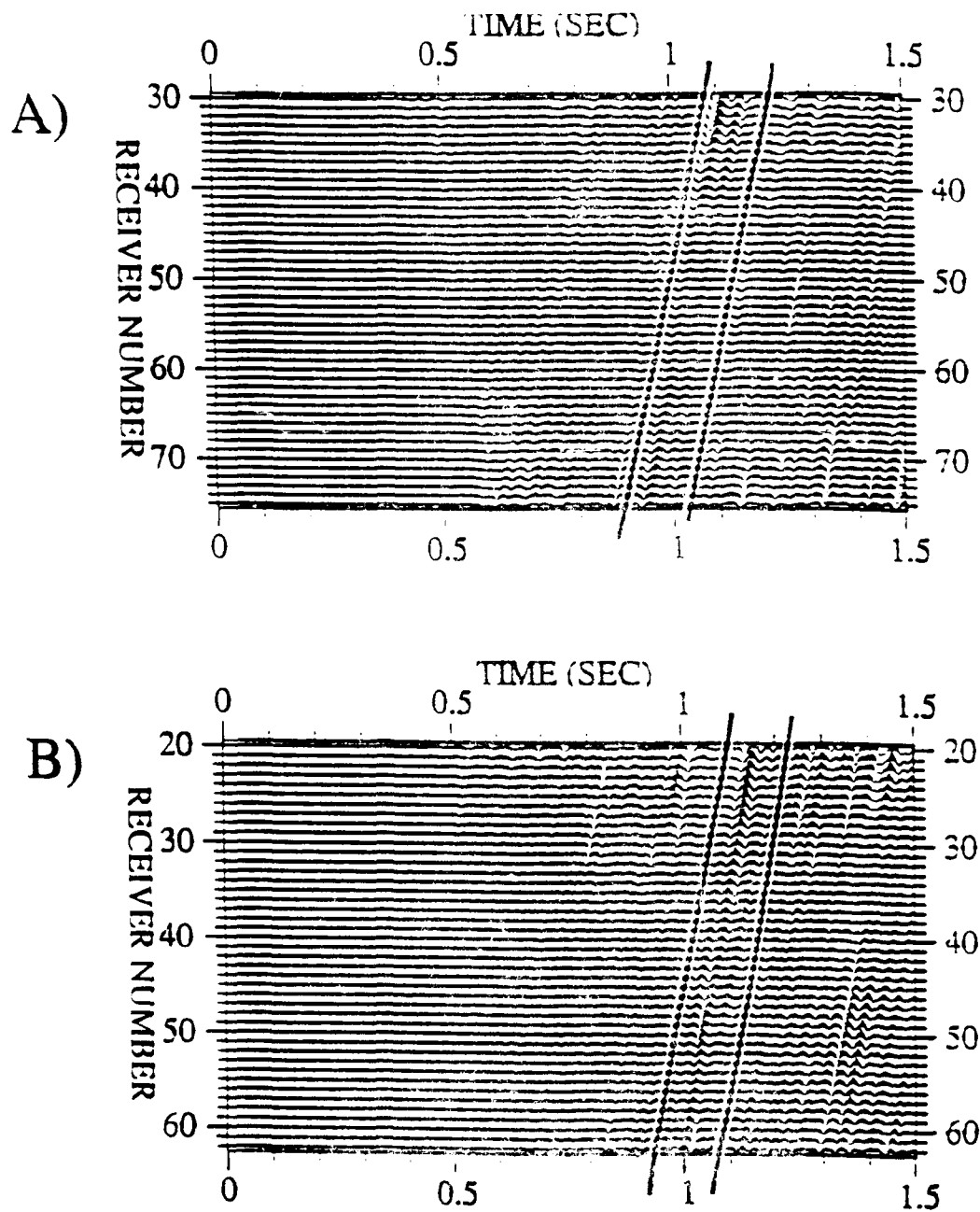
Figure 21: Upgoing wavefields for the zero offset source (above) and the A offset (below). The data from Figure 20 were median filtered, then low-pass filtered to obtain these sections. The signal from the H marker is found between the lines indicated on these plots. Note that the zero offset plot is scaled by a factor of three compared to the A offset seismograms, showing that the H marker event is much stronger in the A offset data.
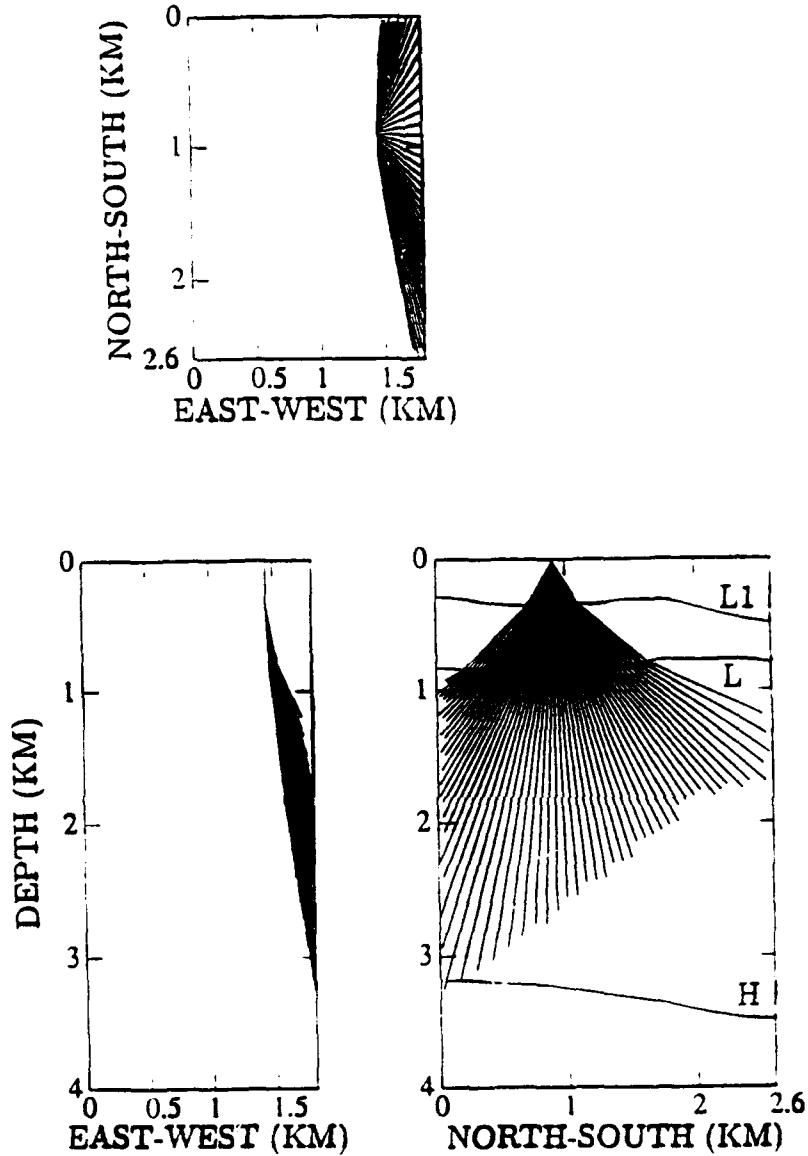
Figure 22: Ray paths for a fan of rays initially in the north-south vertical plane. All three coordinate planes are plotted, and the L1, L and H markers are shown in the appropriate north-south cross section. When the rays encounter the L1 and L horizon, the irregular interfaces bend the ray paths so that they have a strongly three-dimensional propagation showing the complexity of wave propagation in the Larderello region. In a one-dimensional earth model, these rays would have no east-west components. To completely illuminate the H marker, similar fans of rays were traced over all azimuths from both source positions. A) Ray fan from the zero offset source. B) Ray fan from the A offset source.

68
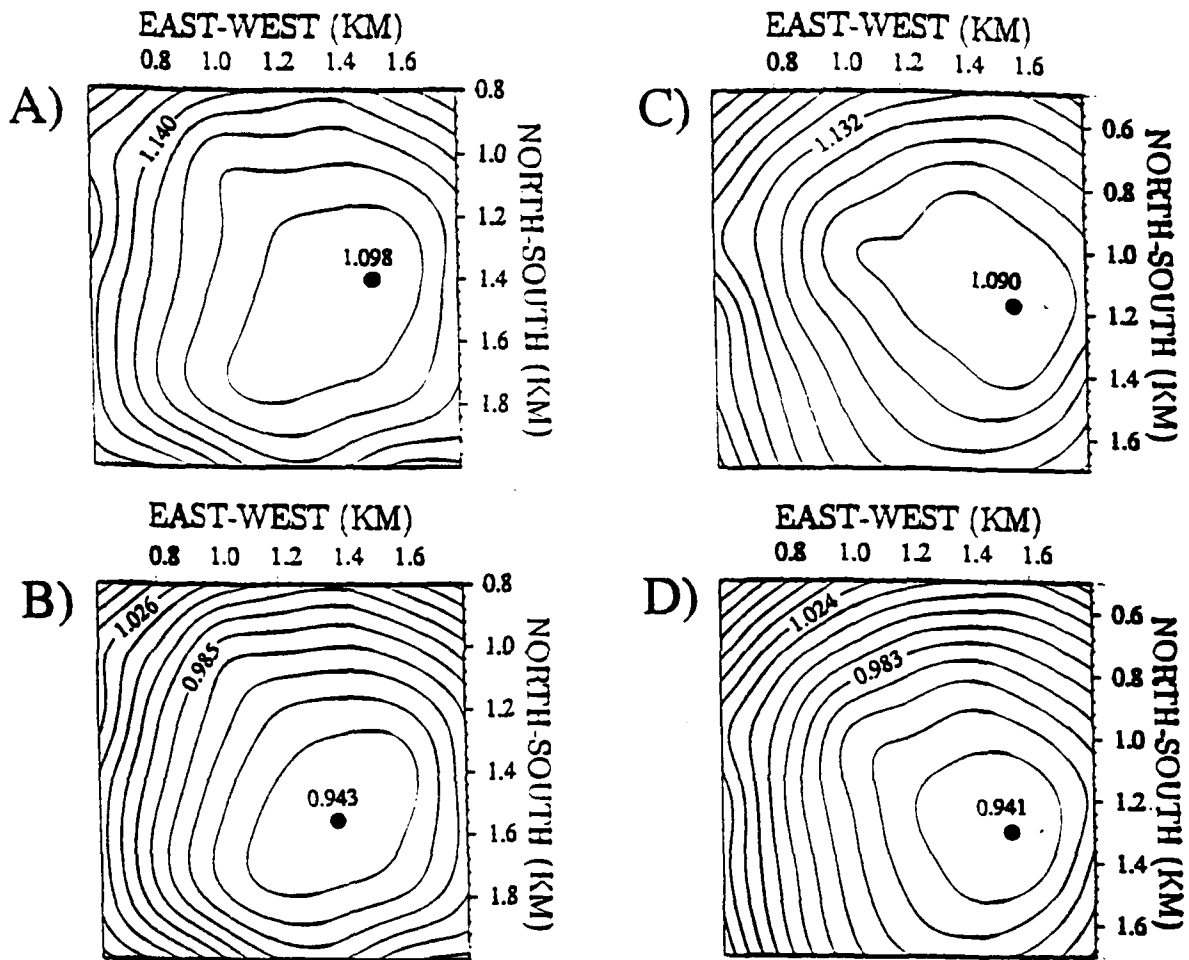
Figure 23: Contour plots of total travel time from the zero offset and A offset sources to the H2 marker and then to receivers at comparable depths. Each contour line bounds a Fresnel zone as described in the text. (A) Total travel time for the zero offset source, receiver 30. (B) Total travel time for the zero offset source, receiver 70. (C) Total travel time for the A offset source, receiver 22. This receiver is at the same depth as receiver 30 for the zero offset source. (D) Total travel time for the A offset source and receiver 62. This receiver is at the same depth as receiver 70 for the zero offset source.

69
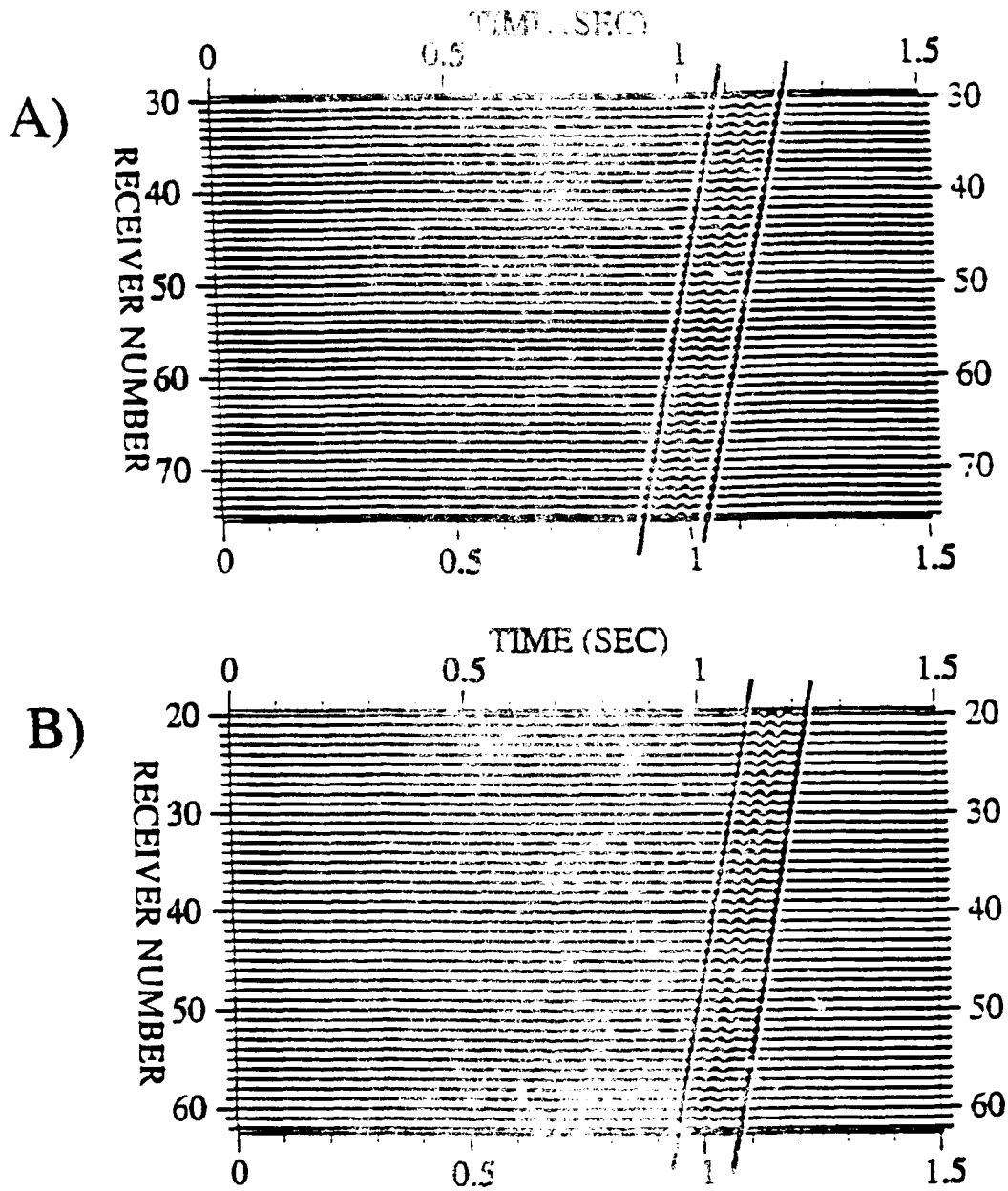
Figure 24: Synthetic seismograms for the Hawaii period 1 described in the text. The results for both the zero offset source receiver and Noffset borehole are shown. The arrival is marked as in the data in Figure 23. The downgoing wavefields were also ray-traced, allowing the synthetics results to be processed in the same way as were the field data.

76

Prof. Thomas Ahrens
Seismological Lab, 252-21
Division of Geological & Planetary Sciences
California Institute of Technology
Pasadena, CA 91125

Prof. Keiiti Aki
Center for Earth Sciences
University of Southern California
University Park
Los Angeles, CA 90089-0741

Prof. Shelton Alexander
Geosciences Department
403 Deike Building
The Pennsylvania State University
University Park, PA 16802

Dr. Ralph Alewine, III
DARPA/NMRO
3701 North Fairfax Drive
Arlington, VA 22203-1714

Prof. Charles B. Archambeau
CIRES
University of Colorado
Boulder, CO 80309

Dr. Thomas C. Bache, Jr.
Science Applications Int'l Corp.
10260 Campus Point Drive
San Diego, CA 92121 (2 copies)

Prof. Muawia Barazangi
Institute for the Study of the Continent
Cornell University
Ithaca, NY 14853

Dr. Jeff Barker
Department of Geological Sciences
State University of New York
 at Binghamton
Vestal, NY 13901

Dr. Douglas R. Baumgardt
ENSCO, Inc
5400 Port Royal Road
Springfield, VA 22151-2388

Dr. Susan Beck
Department of Geosciences
Building #77
University of Arizona
Tuscon, AZ 85721

Dr. T.J. Bennett
S-CUBED
A Division of Maxwell Laboratories
11800 Sunrise Valley Drive, Suite 1212
Reston, VA 22091

Dr. Robert Blandford
AFTAC/TT, Center for Seismic Studies
1300 North 17th Street
Suite 1450
Arlington, VA 22209-2308

Dr. G.A. Bollinger
Department of Geological Sciences
Virginia Polytechnical Institute
21044 Derring Hall
Blacksburg, VA 24061

Dr. Stephen Bratt
Center for Seismic Studies
1300 North 17th Street
Suite 1450
Arlington, VA 22209-2308

Dr. Lawrence Burdick
Woodward-Clyde Consultants
566 El Dorado Street
Pasadena, CA 91109-3245

Dr. Robert Burridge
Schlumberger-Doll Research Center
Old Quarry Road
Ridgefield, CT 06877

Dr. Jerry Carter
Center for Seismic Studies
1300 North 17th Street
Suite 1450
Arlington, VA 22209-2308

Dr. Eric Chael
Division 9241
Sandia Laboratory
Albuquerque, NM 87185

Prof. Vernon F. Cormier
Department of Geology & Geophysics
U-45, Room 207
University of Connecticut
Storrs, CT 06268

Prof. Steven Day
Department of Geological Sciences
San Diego State University
San Diego, CA 92182

1

Marvin Denny
U.S. Department of Energy
Office of Arms Control
Washington, DC 20585

Dr. Cliff Frolich
Institute of Geophysics
8701 North Mopac
Austin, TX 78759

Dr. Zoltan Der
ENSCO, Inc.
5400 Port Royal Road
Springfield, VA 22151-2388

Dr. Holly Given
IGPP, A-025
Scripps Institute of Oceanography
University of California, San Diego
La Jolla, CA 92093

Prof. Adam Dziewonski
Hoffman Laboratory, Harvard University
Dept. of Earth Atmos. & Planetary Sciences
20 Oxford Street
Cambridge, MA 02138

Dr. Jeffrey W. Given
SAIC
10260 Campus Point Drive
San Diego, CA 92121

Prof. John Ebel
Department of Geology & Geophysics
Boston College
Chestnut Hill, MA 02167

Dr. Dale Glover
Defense Intelligence Agency
ATTN: ODT-1B
Washington, DC 20301

Eric Fielding
SNEE Hall
INSTOC
Cornell University
Ithaca, NY 14853

Dr. Indra Gupta
Teledyne Geotech
314 Montgomery Street
Alexanderia, VA 22314

Dr. Mark D. Fisk
Mission Research Corporation
735 State Street
P.O. Drawer 719
Santa Barbara, CA 93102

Dan N. Hagedon
Pacific Northwest Laboratories
Battelle Boulevard
Richland, WA 99352

Prof Stanley Flatte
Applied Sciences Building
University of California, Santa Cruz
Santa Cruz, CA 95064

Dr. James Hannon
Lawrence Livermore National Laboratory
P.O. Box 808
L-205
Livermore, CA 94550

Dr. John Foley
NER-Geo Sciences
1100 Crown Colony Drive
Quincy, MA 02169

Dr. Roger Hansen
HQ AFTAC/TTR
Patrick AFB, FL 32925-6001

Prof. Donald Forsyth
Department of Geological Sciences
Brown University
Providence, RI 02912

Prof. David G. Harkrider
Seismological Laboratory
Division of Geological & Planetary Sciences
California Institute of Technology
Pasadena, CA 91125

Dr. Art Frankel
U.S. Geological Survey
922 National Center
Reston, VA 22092

Prof. Danny Harvey
CIRES
University of Colorado
Boulder, CO 80309

Prof. Donald V. Helmberger
Seismological Laboratory
Division of Geological & Planetary Sciences
California Institute of Technology
Pasadena, CA 91125

Prof. Eugene Herrin
Institute for the Study of Earth and Man
Geophysical Laboratory
Southern Methodist University
Dallas, TX 75275

Prof. Robert B. Herrmann
Department of Earth & Atmospheric Sciences
St. Louis University
St. Louis, MO 63156

Prof. Lane R. Johnson
Seismographic Station
University of California
Berkeley, CA 94720

Prof. Thomas H. Jordan
Department of Earth, Atmospheric &
  Planetary Sciences
Massachusetts Institute of Technology
Cambridge, MA 02139

Prof. Alan Kafka
Department of Geology & Geophysics
Boston College
Chestnut Hill, MA 02167

Robert C. Kemerait
ENSCO, Inc.
445 Pineda Court
Melbourne, FL 32940

Dr. Max Koontz
U.S. Dept. of Energy/DP 5
Forrestal Building
1000 Independence Avenue
Washington, DC 20585

Dr. Richard LaCoss
MIT Lincoln Laboratory, M-200B
P.O. Box 73
Lexington, MA 02173-0073

Dr. Fred K. Lamb
University of Illinois at Urbana-Champaign
Department of Physics
1110 West Green Street
Urbana, IL 61801

Prof. Charles A. Langston
Geosciences Department
403 Deike Building
The Pennsylvania State University
University Park, PA 16802

Jim Lawson, Chief Geophysicist
Oklahoma Geological Survey
Oklahoma Geophysical Observatory
P.O. Box 8
Leonard, OK 74043-0008

Prof. Thorne Lay
Institute of Tectonics
Earth Science Board
University of California, Santa Cruz
Santa Cruz, CA 95064

Dr. William Leith
U.S. Geological Survey
Mail Stop 928
Reston, VA 22092

Mr. James F. Lewkowicz
Phillips Laboratory/GPEH
Hanscom AFB, MA 01731-5000(2 copies)

Mr. Alfred Lieberman
ACDA/VI-OA State Department Building
Room 5726
320-21st Street, NW
Washington, DC 20451

Prof. L. Timothy Long
School of Geophysical Sciences
Georgia Institute of Technology
Atlanta, GA 30332

Dr. Randolph Martin, III
New England Research, Inc.
76 Olcott Drive
White River Junction, VT 05001

Dr. Robert Masse
Denver Federal Building
Box 25046, Mail Stop 967
Denver, CO 80225

Dr. Gary McCartor
Department of Physics
Southern Methodist University
Dallas, TX 75275

Prof. Thomas V. McEvilly
Seismographic Station
University of California
Berkeley, CA 94720

Prof. John A. Orcutt
IGPP, A-025
Scripps Institute of Oceanography
University of California, San Diego
La Jolla, CA 92093

Dr. Art McGarr
U.S. Geological Survey
Mail Stop 977
U.S. Geological Survey
Menlo Park, CA 94025

Prof. Jeffrey Park
Kline Geology Laboratory
P.O. Box 6666
New Haven, CT 06511-8130

Dr. Keith L. McLaughlin
S-CUBED
A Division of Maxwell Laboratory
P.O. Box 1620
La Jolla, CA 92038-1620

Dr. Howard Patton
Lawrence Livermore National Laboratory
L-025
P.O. Box 808
Livermore, CA 94550

Stephen Miller & Dr. Alexander Florence
SRI International
333 Ravenswood Avenue
Box AF 116
Menlo Park, CA 94025-3493

Dr. Frank Pilotte
HQ AFTAC/TT
Patrick AFB, FL 32925-6001

Prof. Bernard Minster
IGPP, A-025
Scripps Institute of Oceanography
University of California, San Diego
La Jolla, CA 92093

Dr. Jay J. Pulli
Radix Systems, Inc.
2 Taft Court, Suite 203
Rockville, MD 20850

Prof. Brian J. Mitchell
Department of Earth & Atmospheric Sciences
St. Louis University
St. Louis, MO 63156

Dr. Robert Reinke
ATTN: FCTVTD
Field Command
Defense Nuclear Agency
Kirtland AFB, NM 87115

Mr. Jack Murphy
S-CUBED
A Division of Maxwell Laboratory
11800 Sunrise Valley Drive, Suite 1212
Reston, VA 22091 (2 Copies)

Prof. Paul G. Richards
Lamont-Doherty Geological Observatory
 of Columbia University
Palisades, NY 10964

Dr. Keith K. Nakanishi
Lawrence Livermore National Laboratory
L-025
P.O. Box 808
Livermore, CA 94550

Mr. Wilmer Rivers
Teledyne Geotech
314 Montgomery Street
Alexandria, VA 22314

Dr. Carl Newton
Los Alamos National Laboratory
P.O. Box 1663
Mail Stop C335, Group ESS-3
Los Alamos, NM 87545

Dr. George Rothe
HQ AFTAC/TTR
Patrick AFB, FL 32925-6001

Dr. Bao Nguyen
HQ AFTAC/TTR
Patrick AFB, FL 32925-6001

Dr. Alan S. Ryall, Jr.
DARPA/NMRO
3701 North Fairfax Drive
Arlington, VA 22209-1714

Dr. Richard Sailor
TASC, Inc.
55 Walkers Brook Drive
Reading, MA 01867

Donald L. Springer
Lawrence Livermore National Laboratory
L-025
P.O. Box 808
Livermore, CA 94550

Prof. Charles G. Sammis
Center for Earth Sciences
University of Southern California
University Park
Los Angeles, CA 90089-0741

Dr. Jeffrey Stevens
S-CUBED
A Division of Maxwell Laboratory
P.O. Box 1620
La Jolla, CA 92038-1620

Prof. Christopher H. Scholz
Lamont-Doherty Geological Observatory
 of Columbia University
Palisades, CA 10964

Lt. Col. Jim Stobie
ATTN: AFOSR/NL
Bolling AFB
Washington, DC 20332-6448

Dr. Susan Schwartz
Institute of Tectonics
1156 High Street
Santa Cruz, CA 95064

Prof. Brian Stump
Institute for the Study of Earth & Man
Geophysical Laboratory
Southern Methodist University
Dallas, TX 75275

Secretary of the Air Force
(SAFRD)
Washington, DC 20330

Prof. Jeremiah Sullivan
University of Illinois at Urbana-Champaign
Department of Physics
1110 West Green Street
Urbana, IL 61801

Office of the Secretary of Defense
DDR&E
Washington, DC 20330

Prof. L. Sykes
Lamont-Doherty Geological Observatory
 of Columbia University
Palisades, NY 10964

Thomas J. Sereno, Jr.
Science Application Int'l Corp.
10260 Campus Point Drive
San Diego, CA 92121

Dr. David Taylor
ENSCO, Inc.
445 Pineda Court
Melbourne, FL 32940

Dr. Michael Shore
Defense Nuclear Agency/SPSS
6801 Telegraph Road
Alexandria, VA 22310

Dr. Steven R. Taylor
Los Alamos National Laboratory
P.O. Box 1663
Mail Stop C335
Los Alamos, NM 87545

Dr. Matthew Sibol
Virginia Tech
Seismological Observatory
4044 Derring Hall
Blacksburg, VA 24061-0420

Prof. Clifford Thurber
University of Wisconsin-Madison
Department of Geology & Geophysics
1215 West Dayton Street
Madison, WS 53706

Prof. David G. Simpson
IRIS, Inc.
1616 North Fort Myer Drive
Suite 1440
Arlington, VA 22209

Prof. M. Nafi Toksoz
Earth Resources Lab
Massachusetts Institute of Technology
42 Carleton Street
Cambridge, MA 02142

Dr. Larry Turnbull
CIA-OSWR/NED
Washington, DC 20505

DARPA/RMO/SECURITY OFFICE
3701 North Fairfax Drive
Arlington, VA 22203-1714

Dr. Gregory van der Vink
IRIS, Inc.
1616 North Fort Myer Drive
Suite 1440
Arlington, VA 22209

HQ DNA
ATTN: Technical Library
Washington, DC 20305

Dr. Karl Veith
EG&G
5211 Auth Road
Suite 240
Suitland, MD 20746

Defense Intelligence Agency
Directorate for Scientific & Technical Intelligence
ATTN: DTIB
Washington, DC 20340-6158

Prof. Terry C. Wallace
Department of Geosciences
Building #77
University of Arizona
Tuscon, AZ 85721

Defense Technical Information Center
Cameron Station
Alexandria, VA 22314 (2 Copies)

Dr. Thomas Weaver
Los Alamos National Laboratory
P.O. Box 1663
Mail Stop C335
Los Alamos, NM 87545

TACTEC
Battelle Memorial Institute
505 King Avenue
Columbus, OH 43201 (Final Report)

Dr. William Wortman
Mission Research Corporation
8560 Cinderbed Road
Suite 700
Newington, VA 22122

Phillips Laboratory
ATTN: XPG
Hanscom AFB, MA 01731-5000

Prof. Francis T. Wu
Department of Geological Sciences
State University of New York
 at Binghamton
Vestal, NY 13901

Phillips Laboratory
ATTN: GPE
Hanscom AFB, MA 01731-5000

AFTAC/CA
(STINFO)
Patrick AFB, FL 32925-6001

Phillips Laboratory
ATTN: TSML
Hanscom AFB, MA 01731-5000

DARPA/PM
3701 North Fairfax Drive
Arlington, VA 22203-1714

Phillips Laboratory
ATTN: SUL
Kirtland, NM 87117 (2 copies)

DARPA/RMO/RETRIEVAL
3701 North Fairfax Drive
Arlington, VA 22203-1714

Dr. Michel Bouchon
I.R.I.G.M.-B.P. 68
38402 St. Martin D'Heres
Cedex, FRANCE

Dr. Michel Campillo
Observatoire de Grenoble
I.R.I.G.M.-B.P. 53
38041 Grenoble, FRANCE

Dr. Jorg Schlittenhardt
Federal Institute for Geosciences & Nat'l Res.
Postfach 510153
D-3000 Hannover 51, GERMANY

Dr. Kin Yip Chun
Geophysics Division
Physics Department
University of Toronto
Ontario, CANADA

Dr. Johannes Schweitzer
Institute of Geophysics
Ruhr University/Bochum
P.O. Box 1102148
4360 Bochum 1, GERMANY

Prof. Hans-Peter Harjes
Institute for Geophysic
Ruhr University/Bochum
P.O. Box 102148
4630 Bochum 1, GERMANY

Prof. Eystein Husebye
NTNF/NORSAR
P.O. Box 51
N-2007 Kjeller, NORWAY

David Jepsen
Acting Head, Nuclear Monitoring Section
Bureau of Mineral Resources
Geology and Geophysics
G.P.O. Box 378, Canberra, AUSTRALIA

Ms. Eva Johannisson
Senior Research Officer
National Defense Research Inst.
P.O. Box 27322
S-102 54 Stockholm, SWEDEN

Dr. Peter Marshall
Procurement Executive
Ministry of Defense
Blacknest, Brimpton
Reading FG7-FRS, UNITED KINGDOM

Dr. Bernard Massinon, Dr. Pierre Mechler
Societe Radiomana
27 rue Claude Bernard
75005 Paris, FRANCE (2 Copies)

Dr. Svein Mykkeltveit
NTNT/NORSAR
P.O. Box 51
N-2007 Kjeller, NORWAY (3 Copies)

Prof. Keith Priestley
University of Cambridge
Bullard Labs, Dept. of Earth Sciences
Madingley Rise, Madingley Road
Cambridge CB3 OEZ, ENGLAND